SPECTRALLY-RESOLVED DIFFERENTIAL REFLECTIVITY RESPONSE OF GaMnAs

by

Tristan de Boer

Submitted in partial fulfillment of the
requirements for the degree of
Master of Science

at

Dalhousie University
Halifax, Nova Scotia
August 2011

© Copyright by Tristan de Boer, 2011

DALHOUSIE UNIVERSITY

PHYSICS AND ATMOSPHERIC SCIENCE

The undersigned hereby certify that they have read and recommend to the Faculty of Graduate Studies for acceptance a thesis entitled "SPECTRALLY-RESOLVED DIFFERENTIAL REFLECTIVITY RESPONSE OF GaMnAs" by Tristan de Boer in partial fulfillment of the requirements for the degree of Master of Science.

Dated: August 26, 2011

Supervisor: ____________________

Readers: ____________________

____

DALHOUSIE UNIVERSITY

DATE: August 26, 2011

AUTHOR: Tristan de Boer

TITLE: SPECTRALLY-RESOLVED DIFFERENTIAL REFLECTIVITY RESPONSE OF GaMnAs

DEPARTMENT OR SCHOOL: Physics and Atmospheric Science

DEGREE: M.Sc. CONVOCATION: October YEAR: 2011

Permission is herewith granted to Dalhousie University to circulate and to have copied for non-commercial purposes, at its discretion, the above title upon the request of individuals or institutions. I understand that my thesis will be electronically available to the public.

The author reserves other publication rights, and neither the thesis nor extensive extracts from it may be printed or otherwise reproduced without the author's written permission.

The author attests that permission has been obtained for the use of any copyrighted material appearing in the thesis (other than brief excerpts requiring only proper acknowledgement in scholarly writing), and that all such use is clearly acknowledged.

Signature of Author

For Krista.

Table of Contents

List of Tables . . . . **vii**

List of Figures . . . . **viii**

Abstract . . . . **xi**

List of Abbreviations and Symbols Used . . . . **xii**

Acknowledgements . . . . **xiii**

Chapter 1 Introduction **1**

Chapter 2 Background Information **5**

2.1 Chapter Outline 5

2.2 Review of Bulk Semiconductor Physics 5

2.3 Defects in GaAs 6
2.3.1 Low Temperature Grown GaAs 7

2.4 Electronic Structure of GaMnAs 10

2.5 Literature Review 12

2.6 Signal Contributions to Pump Probe 15
2.6.1 Phase Space Filling 15
2.6.2 Free Carrier Absorption 17
2.6.3 Defect-Related Absorption 18
2.6.4 Band Gap Renormalization 20
2.6.5 Sample Pump Probe Results: High Temperature Grown Undoped GaAs 21

Chapter 3 Overview of Experiments **23**

3.1 Chapter Outline 23

3.2 Samples 23

3.3 Pump Probe Spectroscopy 24

3.4 Experimental Apparatus 25

3.5 Laser Spot Size and Excitation Density 28

Chapter 4 Results and Discussion **29**

4.1 Chapter Outline 29

4.2 Spectrally-Resolved Differential Reflectivity Experiments in GaMnAs 29

4.3 Calculated Differential Reflection Signals 38

4.4 Discussion 45

Chapter 5 Conclusions and Future Work **49**

Appendix A Excited Carrier Density Calculation Details **51**

A.1 Spot Size Calculation 51

A.2 Carrier Density Calculation 51

Bibliography **53**

List of Tables

Table 3.1 Summary of physical characteristics of samples studied. 23

Table 4.1 Estimated changes to the band gap of low-temperature grown p-type GaAs due to the Moss Burstein shift, band gap renormalization and coupling to defects. 46

List of Figures

Figure 1.1 A diagram of GaMnAs. Ga, Mn and As lattice sites are as indicated. The Mn atom can either substitute at a Ga site or act as an interstitial defect. A wavefunction of the delocalized hole is represented as a gray ellipse and the hole spin indicated with a yellow arrow. 2

Figure 2.1 (a) GaAs bandstructure obtained using a pseudopotential calculation [1]. (b) Simplified band structure of a direct bandgap semiconductor. C denotes the conduction band, HH the heavy hole band, LH the light hole band and SO the split-off band. Each of these bands is doubly degenerate including the spin degree of freedom. 6

Figure 2.2 Simplified band structure and optical transitions of a heavily doped p-type direct band gap semiconductor at zero temperature. E_g denotes the transition from the top of the valence band to the bottom of the conduction band. E_{LH-C} (E_{HH-C}) denotes the lowest energy transition measurable in optical absorption experiments involving the LH (HH) band. 8

Figure 2.3 Schematic diagram of the electronic structure near the band gap of LT-GaAs. Shown are deep defects near the center of the band gap and band tails states near the conduction and valence band edges. 9

Figure 2.4 A schematic diagram of the electronic band structure of GaMnAs for low concentrations of Mn. As_{Ga} states form a deep donor band near the midgap. Band tail states caused by potential fluctuations in the crystal are shown. Interstitial Mn states produce a shallow donor level, while states associated with substitutional Mn form exist close to the top of the valence band. 11

Figure 2.5 R_{Hall} versus applied magnetic field curves on an LT-grown InMnAs sample at 22.5 K. Various gate voltages were applied to the sample, as indicated [2]. The inset shows the same curves at higher magnetic fields. 12

Figure 2.6 (A) shows a band structure diagram of LT-GaAs. (B) shows a band structure diagram of GaMnAs in the impurity band model. (C) shows a band structure diagram of GaMnAs in the valence band model. The thin and thick arrows denote allowed optical transitions. Diagram taken from [3]. 13

Figure 2.7 Schematic diagram of defect-related absorption processes in a direct band gap semiconductor. After inital excitation by the pump, excited carriers get trapped to defect states where they can be re-excited by the probe to the conduction band. 19

Figure 2.8 (a) Room temperature absorption spectra of bulk GaAs with excitation powers between 0 and 50 mW on a 15 μm spot size. (b) Δn extracted from data in (a) via nonlinear KKR [4]. . . . 22

Figure 3.1 Schematic diagram of pump probe spectroscopy, shown in the differential reflection geometry. The time interval $\Delta\tau$ between the pump and probe pulses on the sample can be controlled by varying the optical path length of the probe with respect to the pump. 25

Figure 3.2 Layout of the laser system on the optical table. 26

Figure 3.3 Schematic of the experimental apparatus. The green path represents the pump, the red path the probe and the blue the post-sample reflected probe. 27

Figure 4.1 Differential reflection of SI GaAs at probe energy 1.652 eV at (a) short delays and (b) long delays. 31

Figure 4.2 Differential reflection of the SI GaAs sample. Probe energy is shown in the horizontal axis while delay is shown on the vertical axis for (a) short delays and (b) for long delays. The colour corresponds to the DRR signal level at a given energy and delay. The band gap of GaAs at 80 K is indicated with a blue line. The fast dynamics at early time scales are not captured in these 3D plots due to the finite mesh used to generate the plot. 33

Figure 4.3 Differential reflection of 150 nm thick GaMnAs at probe energy 1.652 eV at (a) short delays and (b) long delays. 34

Figure 4.4 Differential reflection of the G030-3 GaMnAs sample. Probe energy is shown in the horizontal axis while delay is shown on the vertical axis for (a) short delays and (b) for long delays. The colour corresponds to the DRR signal level at a given energy and delay. The band gap of GaAs at 80 K is indicated with a blue line. The fast dynamics at early time scales are not captured in these 3D plots due to the finite mesh used to generate the plot. 35

Figure 4.5 Differential reflection of the (a) 150 nm GaMnAs sample and (b) LT GaAs sample. Probe energy is shown in the horizontal axis while delay is shown on the vertical axis. The colour corresponds to the DRR signal level at a given energy and delay. The band gap of GaAs at 80 K is indicated with a blue line. The fast dynamics at early time scales are not captured in these 3D plots due to the finite mesh used to generate the plot. . . . 37

Figure 4.6 Differential reflection of the (a) 150 nm GaMnAs sample and (b) 20 nm GaMnAs sample. Probe energy is shown in the horizontal axis while delay is shown on the vertical axis. The colour corresponds to the DRR signal level at a given energy and delay. The band gap of GaAs at 80 K is indicated with a blue line. The fast dynamics at early time scales are not captured in these 3D plots due to the finite mesh used to generate the plot. 39

Figure 4.7 Calculated pump-induced changes in the extinction coefficient, index of refraction and differential reflection are shown for various signal contributions in the first, second and third columns respectively. Changes due to bandfilling, FCA, DA and BGR are shown in the first through fourth rows respectively. A carrier density of $2 \times 10^{18}\text{cm}^{-3}$ was used in these calculations. . . 41

Figure 4.8 Theoretical plots of the DRR response due to (a) BGR (dashed line) and bandfilling (solid line) (b) FCA and (c) DA are shown on the left. On the right, a comparison of (d) bandfilling and the DRR response of SI GaAs at 500 ps is shown as well as (e) the DRR response of the 20 nm and 150 nm GaMnAs samples with a DRR response where bandfilling, FCA and DA are included. The strength of the DA response was the only fitting parameter used. 42

Figure 4.9 A schematic diagram of pump-induced electronic transitions in GaMnAs in the impurity band picture. After the pump excites electrons to the conduction band from the valence band, the injected holes could get trapped in the impurity band. Once there, two absorption processes could be expected: (i) a state filling signal could be expected at energies below the band gap as there would be a reduction in the available transitions from the IB to the CB; (ii) an additional absorption mechanism due to VB-IB transitions. 48

Abstract

Spectrally-resolved differential reflectivity experiments on GaMnAs over a broad spectral range (1.4-2.0 eV) are presented, representing the first such measurements in a III-Mn-V diluted magnetic semiconductor. Comparison of the measured nonlinear spectra with results in GaAs and LT-GaAs, together with calculations of the pump probe signal contributions, has allowed an unambiguous identification of the relevant scattering and relaxation processes for optically-excited carriers in this material system. The measured spectra indicate a clear blue shift in the nonlinear optical response, providing support for the valence band model of ferromagnetism in III-Mn-V diluted magnetic semiconductors.

List of Abbreviations and Symbols Used

Å	Angstrom (units of length)
BGR	Band gap renormalization
°C	Degrees Celsius (units of temperature)
DA	Defect absorption
DMS	Dilute magnetic semiconductor
DRR	Differential reflection
E_F	Fermi energy
E_g	Band gap energy
FCA	Free carrier absorption
eV	Electron Volts (units of energy)
GaAs	Gallium arsenide
GaMnAs	Gallium manganese arsenide
GVD	Group velocity dispersion
HH	Heavy hole
IB	Impurity band
InMnAs	Indium manganese arsenide
K	Degrees Kelvin (units of temperature)
KKR	Kramers-Krönig relations
LH	Light hole
LT-GaAs	Low temperature grown gallium arsenide
MBE	Molecular beam epitaxy
MCD	Magnetic circular dichroism
PSF	Phase space filling
SI GaAs	Semi-insulating GaAs
SO	Split-off
τ_{therm}	Thermalization time
T_C	Curie temperature
TR-PL	Time-resolved photo luminescence
VB	Valence band

Acknowledgements

I would like to thank my supervisor, Dr. Kimberley Hall, for all of the help, guidance and opportunity she has offered me. I would also like to thank Vit Novak of the Institute of Physics at the Czech Academy of Sciences for growing the samples used in this experiment.

I would like to thank my fellow members of the Hall research group, particularly Angela Gamouras who was always happy to assist me with the laser system. I would also like to thank Reuble Mathew, Sam March, Aaron Maszko and Murat Yildirim for their friendship, moral support, helpful discussion and assistance.

I would also like to thank the staff of the Department of Physics and Atmospheric Science at Dalhousie, especially Kevin Borgel, John Noddin, Ted Monchesky, Barbara Gauvin, Krista Cullymore, Anne Murphy, Tanya Timmins and Jennifer Currie for all the discussion and assistance they have offered.

Last but not least I would like to thank my family for all their unwavering support and encouragement throughout my studies.

Chapter 1

Introduction

Diluted magnetic semiconductors (DMS) are a new class of materials which have been the subject of intense experimental interest because of their potential role in emerging semiconductor technology. DMS are traditional semiconductors that have been doped with magnetic impurities. (For example, the majority of studies have been made on gallium arsenide (GaAs) doped with manganese (Mn).) DMS materials exhibit a unique kind of ferromagnetism in which the local magnetic moments created by the dopants interact via spin-dependent coupling to delocalized carriers (holes). This so-called *carrier-mediated ferromagnetism* gives these materials a unique combination of semiconducting and magnetic properties. In particular, one can control the magnetic characteristics by varying the carrier density, just as electrical characteristics are controlled in traditional semiconductors by varying the carrier density using, for example, electrical gates or optical excitation. This feature makes these materials of interest for developing new semiconductor devices that would exploit the magnetic and electronic properties simultaneously.

GaAs is extensively used in industry for optoelectronic devices, such as photodetectors, and in high-speed electronics. It has therefore been extremely well-characterized, representing a good starting point for understanding the electronic and optical properties of GaMnAs. For this reason, GaMnAs has become the prototype DMS system. With the development of nonequilibrium growth techniques such as molecular beam epitaxy (MBE), Mn can be doped into GaAs (GaMnAs) at relatively high concentrations (up to $\sim$10%). When the Mn ion substitutes for Ga, it forms a Mn^{2+} ion and acts as a p-type dopant, leading to the generation of a hole (see Figure 1.1). The holes couple anti-ferromagnetically to the Mn ions via the exchange interaction. As a result, even though the Mn ions are too far apart for their magnetic moments to interact directly with each other (hence the name "diluted"), spin-dependent Mn-hole coupling leads to long range ferromagnetic coupling between the local Mn moments.

GaMnAs typically becomes ferromagnetic when $\approx 1.5\%$ of the Ga ions have been replaced with Mn ions. Although no room-temperature ferromagnetic GaMnAs samples have yet been grown, steady progress has been made in raising the Curie temperature from an initial 60 K [5] to 185 K [6]. Studies in this material are providing a basis for understanding (and engineering) the entire class of III-Mn-V DMS.

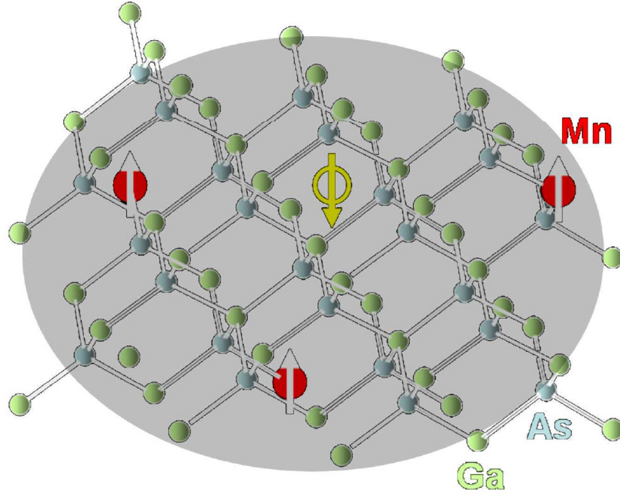

Figure 1.1: A diagram of GaMnAs. Ga, Mn and As lattice sites are as indicated. The Mn atom can either substitute at a Ga site or act as an interstitial defect. A wavefunction of the delocalized hole is represented as a gray ellipse and the hole spin indicated with a yellow arrow.

Carrier-mediated ferromagnetism in DMS materials is distinct from ferromagnetism in metals because the magnetic properties of the sample (e.g. coercive field strength [7], Curie temperature (T_C) [2]) can be controlled using electrical gating or optical excitation. This leads to a whole host of possible directions for the development of magneto-sensitive electronic or photonic devices. For example, a notable feature of DMS is their relatively large g-factor [8]. A commercial Faraday isolator based on a II-VI DMS has already been developed [9]. A variety of proof-of-principle magnetosensitive electronic devices have also been demonstrated, including spin-dependent resonant tunneling diodes,[10] magnetic tunnel junctions [11] and spin-polarized light-emitting diodes [12, 13]. Other proposed devices that would benefit from the use of a DMS semiconductor as a ferromagnetic contact include spin-sensitive field effect

transistors [14, 15, 16], laser diodes with polarised output [17], low-power electrically-controlled nonvolatile memory, optically addressable nonvolatile memory as well as devices which don't have to 'boot-up'[17]. A particularly attractive feature of DMS materials for such devices is that the integration of magnetic and electronic functionality is seamless, at least in principle, because only semiconductors materials are required.

Of crucial importance to device development is a strong understanding of the electronic properties of a material, including the carrier dynamics and the electronic structure. In particular, an active controversy exists with respect to the position of the Fermi level, leading to a considerable body of research over the past decade aimed at understanding the fundamental properties of GaMnAs [18, 19, 20]. In one interpretation [21, 20] the holes in GaMnAs reside in the valence band, similar to regular p-doped GaAs [22], and the Fermi energy resides below the valence band edge. In an alternative interpretation [23], the holes (and the Fermi level) reside in an impurity band above the valence band edge. Linear optical studies to date have yielded conflicting results [18, 24, 20]. As demonstrated in this thesis work, this is a subject to which nonlinear pump probe spectroscopy can contribute.

In this thesis, pump probe spectroscopy is used to study the carrier dynamics and to gain insight into the electronic structure of GaMnAs. Pump probe spectroscopy is a technique where an ultrafast optical pulse, known as the pump, is used to excite a material. The pump-induced change in an optical property of the material (e.g. transmissivity or reflectivity) is studied using a second pulse, known as the probe. Time-resolved dynamics can be studied by varying the time delay between the pump and the probe pulses. Pump-probe spectroscopy provides very fine time resolution, limited only by the pulse duration ($\sim$100 fs in this work). Pump probe techniques have been used to study a variety of dynamic phenomena in semiconductor materials, for example, carrier relaxation [25], intervalley scattering [26] and energy loss rates [27]. These techniques have also been applied to the study of carrier relaxation and optically-induced phenomena in ferromagnetic metals [28, 29].

In this thesis, differential reflectivity experiments are performed on GaMnAs. The novel feature of the work is the application of a femtosecond white light continuum

probe to observe the nonlinear optical response over a wide range of photon energies encompassing the band gap. The measured results provide a comprehensive understanding of the carrier dynamics in this material, and provide new information regarding the spectral dependence of different sources of the measured nonlinarity. This work also illustrates for the first time that pump probe (nonlinear) spectroscopy provides a powerful new tool for studying the electronic structure of GaMnAs. The results also provide insight into the mechanism of ferromagnetic coupling in this system.

This thesis is structured as follows: Chapter two contains a discussion of the basic properties of GaAs and GaMnAs. The limitations of current understanding of the electronic structure of GaMnAs are highlighted. The way in which pump probe spectroscopy can contribute to an improved understanding is also described. Chapter three contains an introduction to experimental details, including the physical properties of the samples studied, the experimental technique, and the apparatus used. Chapter four contains a discussion of the results of the experiments. The results of theoretical simulations of the measured spectra is also provided in Chapter Four. Chapter five contains a summary of the major conclusions and a discussion of future work.

Chapter 2

Background Information

2.1 Chapter Outline

This chapter begins with an introduction to the basic properties of GaAs (Sec. 2.2) as well as GaAs with excess holes and low-temperature grown GaAs (Sec. 2.3). Section 2.4 contains an introduction to the electronic structure of GaMnAs, emphasizing the properties in the dilute limit of Mn doping. A brief literature review is presented in Sec. 2.5, in which the controversy that exists regarding the band structure when the Mn content is increased beyond a few % is highlighted. This motivates the use of pump-probe spectroscopy to study the nonlinear optical response of GaMnAs. Understanding the results in this thesis requires an introduction to various contributions to pump-probe signals. These signal contributions are introduced in Sec. 2.6.

2.2 Review of Bulk Semiconductor Physics

In a solid, the electronic properties of the material will be determined by the electronic band structure. GaAs is a direct bandgap III-V semiconductor with a zinc-blende crystal structure. In a semiconductor, the valence band is the highest fully occupied electron band at $T = 0$ K, while the conduction band is the first unoccupied band, separated from the filled valence band by the band gap E_g. The band structure of GaAs calculated using a pseudopotential model [1] as well as a simplified band diagram are shown in Fig. 2.1. The valence band is composed of three doubly-degenerate (with spin) bands, the heavy-hole (HH), light-hole (LH) and spin-orbit split-off (SO) bands. The conduction band consists of a single doubly-degenerate (with spin) band. In a direct band-gap semiconductor like GaAs, the critical points of the conduction and valence band are centered at $k = 0$, where k is the electron wavevector. The band gap and Fermi energy level of bulk GaAs at 80 K are 1.5068 eV and 0.7645 eV, respectively. At zero temperature in the absence of optical excitation,

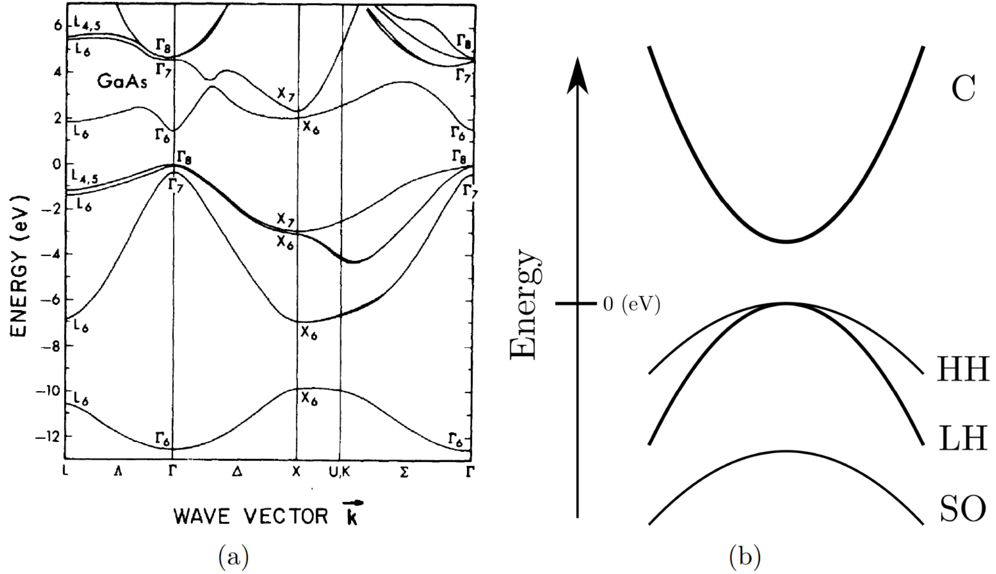

Figure 2.1: (a) GaAs bandstructure obtained using a pseudopotential calculation [1]. (b) Simplified band structure of a direct bandgap semiconductor. C denotes the conduction band, HH the heavy hole band, LH the light hole band and SO the split-off band. Each of these bands is doubly degenerate including the spin degree of freedom.

the Fermi level would reside in the middle of the band gap.

2.3 Defects in GaAs

In order to understand the results of this thesis, it is useful to highlight the basic properties of traditional p-type semiconductors, for which Zn-doped GaAs is considered as an example. In high quality GaAs epilayers, which are grown at elevated temperatures around 500-600 °C, excess holes can be introduced by doping the material with acceptors. In this case, the doped semiconductor is referred to as p-type. The implanted ions lead to an energy level close to but above the valence band edge (for the case of shallow acceptors) [30]. For instance, when GaAs is doped with Zn, the acceptor level resides approximately 30 meV above the valence band edge and has a highly-localized bound hole wavefunction with a Bohr radius of $a_B \approx 18$ Å. At concentrations above 10^{17} cm^{-3} the impurity atom wave functions show substantial overlap and a delocalized band of carriers known as the impurity band forms. At low temperatures, holes are bound to the acceptor atoms, so that the acceptors remain neutral. At sufficiently high temperatures, so that $k_B T$ is comparable to the binding

energy of the acceptor, the acceptor will be ionized and the hole resides in the valence band. With increasing acceptor density the impurity band broadens until, at a sufficiently high concentration, it merges with the valence band [31, 32]. Concurrent with this effect is a narrowing of the bandgap with increasing acceptor concentration [33] due to correlation and exchange interaction effects [34]. For Zn-doped GaAs, the narrowing varies between 20 and 80 meV for acceptor concentrations of between 10^{18} and 10^{20} cm^{-3} respectively. The relevant optical transitions for a highly-doped, p-type semiconductor are shown in Fig. 2.2. The occupation of the valence states near the top of the valence band with holes leads to a modification in the optical absorption of the material: no transitions can occur for photon energies below the threshold for promotion of electrons from occupied states in the valence band to the conduction band. This blue shift in the absorption edge is called the Moss-Burstein effect [35, 36]. Photoluminescence measurements, in contrast, are sensitive to the E_g because in such experiments electrons are promoted through absorption to the conduction band at high energies. These electrons relax to the band edge and recombine with holes at $k = 0$. Thus, photoluminescence is sensitive to shifts in the valence band edge due to band gap renormalization while being insensitive to the Moss-Burstein effect [34] while absorption measurements are affected by both band gap renormalization and the Moss-Burstein effect. Evidence for both the Moss-Burstein effect and band gap narrowing have been observed in absorption measurements of p-doped GaAs [37, 38].

2.3.1 Low Temperature Grown GaAs

Low temperature grown GaAs (LT-GaAs) is GaAs grown using molecular beam epitaxy (MBE) with the substrate held at 200–300 °C. In contrast, high purity MBE grown GaAs [39] is typically grown in the range of 550–650 °C. The reduced surface mobility of As during growth at these low temperatures leads to the incorporation of excess As (as much as 1%–2%). For as-grown and weakly annealed LT-GaAs, the excess As is incorporated primarily in the form of As_{Ga} substitutional antisite point defects. As As is a group V atom, when it replaces Ga (a group III atom) it acts as a double donor. The energies of the associated levels (As^0_{Ga} and As^+_{Ga}) have been studied by several groups [40, 3], and lie near the middle of the band gap of GaAs. As

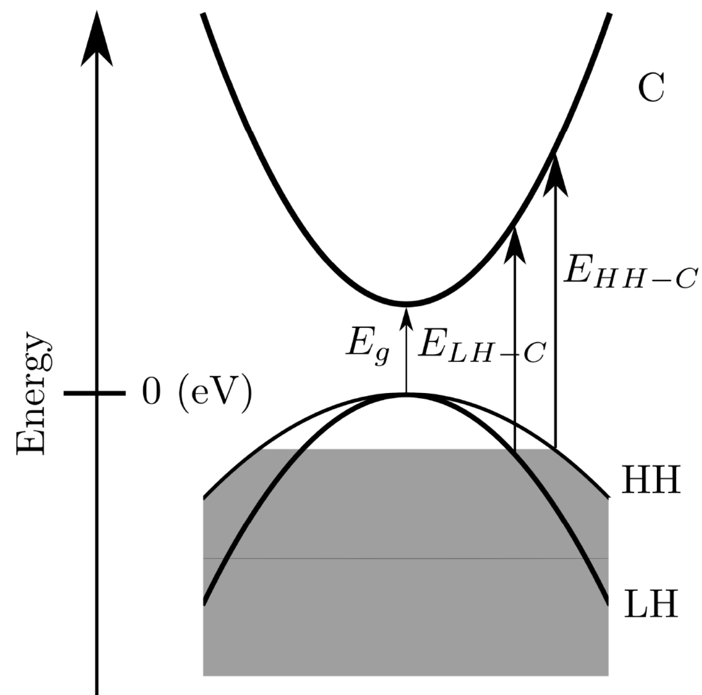

Figure 2.2: Simplified band structure and optical transitions of a heavily doped p-type direct band gap semiconductor at zero temperature. E_g denotes the transition from the top of the valence band to the bottom of the conduction band. E_{LH-C} (E_{HH-C}) denotes the lowest energy transition measurable in optical absorption experiments involving the LH (HH) band.

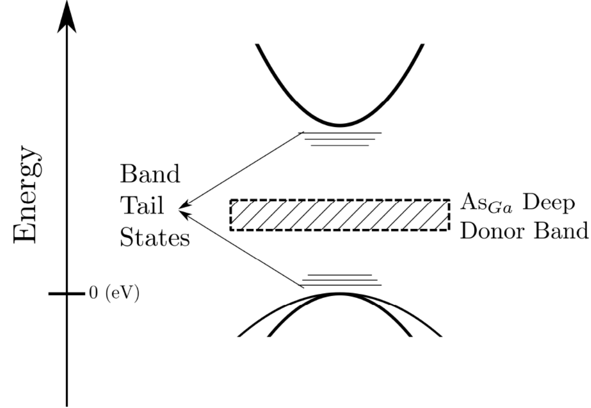

Figure 2.3: Schematic diagram of the electronic structure near the band gap of LT-GaAs. Shown are deep defects near the center of the band gap and band tails states near the conduction and valence band edges.

the density of As_{Ga} is very high, the As_{Ga} levels broaden into a midgap deep donor band. The disorder associated with excess As, which can also exist in the form of As and vacancy clusters [41], leads to shallow potential fluctuations in the crystal. These also produce weakly-localized states in the vicinity of the conduction and valence band edges, referred to as band tails (also known as the Urbach tail in reference to linear absorption experiments). A schematic diagram of LT-GaAs, showing the various defect levels, is shown in Fig. 2.3.

As a result of the midgap donor band, as-grown and weakly annealed LT-GaAs is conducting, although the donor band is still only partially occupied due to vacancies and other defects that lead to compensation. In linear absorption experiments on LT-GaAs, a substantial absorption is observed below the band gap of high-temperature-grown GaAs. In addition, no excitonic features are observed in continuous-wave absorption measurements on LT-GaAs, a finding that has been attributed to inhomogeneous broadening and a very short carrier lifetime in the presence of disorder-related traps [42]. The absorption tail in LT-GaAs is sufficiently strong, in fact, that the band gap energy is impossible to identify.[18] Contributions to the absorption tail below E_g arise from both transitions involving band tail states and the promotion of electrons from the midgap donor band to states in the conduction band. Silverberg et al. showed that transitions from the states deep in the valence band to unoccupied donor band states represents a 10x weaker process compared to the defect to conduction band transitions [43].

LT-GaAs has been extensively studied using pump-probe spectroscopy [39, 44, 42] and spectroscopic studies [45, 46, 47] due to the early interest in this material for applications in all-optical switching. Pump probe experiments suggest that carriers excited to the conduction band relax into either (i) localized band tail states below the band gap via phonon emission which are increasingly localized with decreasing energy or (ii) midgap As-antisite defects. Electrons in the midgap states eventually recombine with holes in the valence band via trap-assisted recombination. Trap saturation can occur if a sufficient quantity of carriers are excited to the conduction band, resulting in a longer overall relaxation time of the material.

2.4 Electronic Structure of GaMnAs

Manganese-doped GaAs (GaMnAs) grown at low temperatures has been the subject of intense experimental interest ever since it was discovered to be ferromagnetic [5, 48]. Since magnetism in this material is mediated by carriers and therefore the magnetic, optical and electronic properties are interconnected [23], it offers the potential to store information in a nonvolatile fashion using a semiconductor platform. Ferromagnetic GaMnAs is grown at low temperatures (similar to LT-GaAs) using MBE. Before the development of low temperature semiconductor growth, experiments involving GaMnAs were hindered by the low solubility of Mn in GaAs. Only by lowering the growth temperature, and hence introducing nonequilibrium growth conditions, can significant quantities of Mn be incorporated into GaMnAs. When GaMnAs is grown at low temperatures, the Mn defects can occupy either substitutional or interstitial sites, where they behave as either acceptors or donors respectively. The outer electron shell configuration of Mn is $3d^5 4s^2$. In GaAs, Ga has three electrons in the valence shell that participate in bonding. When Mn substitutes for Ga (Mn_{Ga}), three of its valence electrons (two from the $4s$ shell and one from the $3d$ shell) participate in bonding. This leaves four d electrons not participating in bonding. Since the lowest energy electron configuration occurs when the atomic spin angular momentum is maximized [49], the substitutional Mn atom will acquire an extra electron, donating a hole to the crystal. If the hole is unbound, the Mn atom it is said to be in an ionized 'A^-' state. If the hole is bound to the Mn atom, the Mn atom it is said to be in the ground 'A^0' state. In the dilute limit this impurity level for GaMnAs is 110 meV

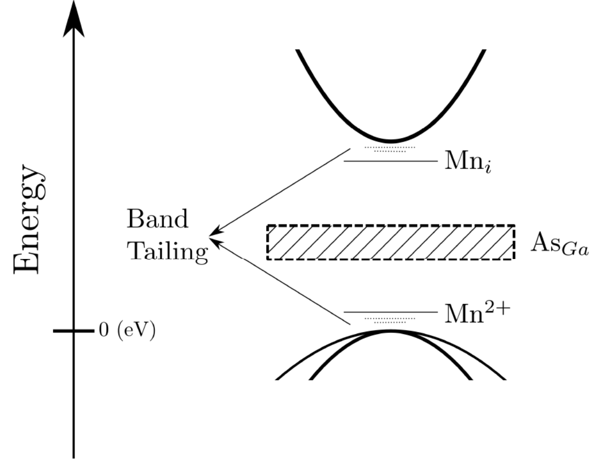

Figure 2.4: A schematic diagram of the electronic band structure of GaMnAs for low concentrations of Mn. As_{Ga} states form a deep donor band near the midgap. Band tail states caused by potential fluctuations in the crystal are shown. Interstitial Mn states produce a shallow donor level, while states associated with substitutional Mn form exist close to the top of the valence band.

above the valence band [50]. For GaMnAs grown at low temperatures and with a low concentration of Mn, the activation energy is closer to 50-60 meV above the valence band [51]. Manganese interstitials form shallow donors which donate two electrons, the binding energy of which is unknown [51]. Mn clustering and MnAs precipitates can also form. A band structure diagram of features in the vicinity of the band gap for low Mn concentrations is shown in Fig. 2.4.

GaMnAs typically becomes ferromagnetic when Mn has a concentration of $x \approx 0.01$, where x is given by $Ga_{1-x}Mn_xAs$. Because of the relatively low concentration of Mn, GaMnAs is known as a dilute magnetic semiconductor (DMS). The ferromagnetism in GaMnAs is due to exchange coupling between localized spins (Mn_{Ga}) and delocalized holes [52, 53]. Since ferromagnetism in GaMnAs is mediated by holes, the intended Mn defect is the substitutional impurity. Since both As antisite defects in LT-GaAs and Mn interstitials contribute excess electrons to GaMnAs, some compensation of the Mn_{Ga} acceptor occurs, and the overall hole concentration is sensitively dependent on the growth process. Correspondingly, the temperature at which ferromagnetic order is lost, known as the Curie temperature (T_C), also depends sensitively on the growth process. Through improving the growth process, the T_C of GaMnAs has risen from 60 K since the discovery of ferromagnetism in this system to 185 K. The highest

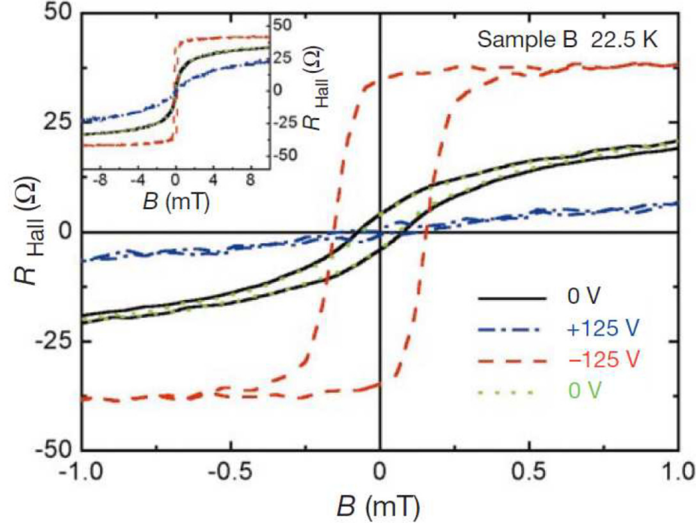

Figure 2.5: R_{Hall} versus applied magnetic field curves on an LT-grown InMnAs sample at 22.5 K. Various gate voltages were applied to the sample, as indicated [2]. The inset shows the same curves at higher magnetic fields.

reported T_C of 185 K was observed in a 23 nm thick GaMnAs epilayer with a nominal Mn doping of 12.5% [6].

2.5 Literature Review

Experimental observation of the carrier-mediated nature of the ferromagnetic coupling in a DMS system was first made in InMnAs using electrical gates [2] and continuous-wave optical excitation [54]. Hall resistance measurements illustrating gate control over the transition temperature are shown in Fig. 2.5. This work stimulated a flurry of research activity aimed at understanding the mechanism of ferromagnetic order in the III-Mn-V DMS, and learning how to optimize the growth conditions to engineer the magnetic characteristics (e.g. increase T_C). The most intensively studied material is GaMnAs, owing to the substantial amount of experience developed by researchers in the past in growing and characterizing this material.

Despite more than a decade of intensive research into the properties of GaMnAs, the band structure and the mechanism of ferromagnetic coupling of this material are still not well understood. GaMnAs shown in Fig. 2.4 is widely accepted for low Mn concentrations. It is also well established that the ferromagnetism in GaMnAs is due to coupling between localized Mn spins via their mutual interaction with holes.

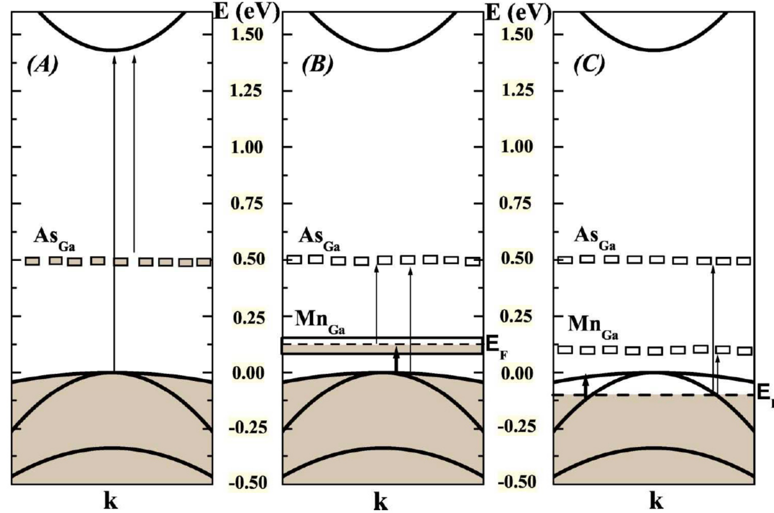

Figure 2.6: (A) shows a band structure diagram of LT-GaAs. (B) shows a band structure diagram of GaMnAs in the impurity band model. (C) shows a band structure diagram of GaMnAs in the valence band model. The thin and thick arrows denote allowed optical transitions. Diagram taken from [3].

However, the evolution of the band structure as Mn is increased beyond the threshold for ferromagnetism is the subject of extensive debate in the literature at the present time. There are two competing proposals regarding the evolution of the band structure. The first proposal is the valence band (VB) model [53, 55, 56, 19] in which the 110 meV Mn impurity level broadens as the Mn concentration is increased, eventually merging with the valence band. The Fermi energy decreases with increasing Mn concentration, eventually going below the VB edge. In this picture the ferromagnetism is described using a Zener mean field model. The second proposal is the impurity band (IB) model in which the holes remain sufficiently localized that the Fermi level remains above the VB edge no matter the Mn concentration [57, 58, 59, 60, 61, 62]. In this picture the ferromagnetism is described using a double exchange model. A simplified band diagram outlining the above is shown in Fig. 2.6. The actual band structure may be a hybrid of these two approaches. For example, the valence band is likely modified by hybridization [3, 63], in contrast to the original valence band picture of Dietl et al. [53] It is also possible that the impurity band states may overlap with the valence band [21], while still retaining their d-character.

Experimental support exists for both proposals. In a series of infrared spectroscopy measurements [64, 3, 65], a strong resonance was observed at 250 meV, which red

shifted with increasing Mn concentration. This redshift is consistent with an IB picture since the IB would be expected to broaden with increasing Mn concentration, resulting in a red shifted transition from the VB to IB. In a separate series of infrared spectroscopy measurements [20], a blue shift of the 250 meV peak was observed with increasing Mn concentration. This is consistent with the valence band picture. Support for both the VB [66, 20] and IB [58, 60, 24] interpretations also exists in magnetic circular dichroism (MCD) experiments. In these experiments, the difference between the reflectivity for left and right circularly-polarized light is measured in DMS samples in which a large magnetic field has been used to bring the easy axis into the growth direction. In this case, an MCD signal is expected at the band edge due to the Zeeman splitting of the band edge states, which is substantially enhanced in the ferromagnetic state. A blue shift of the MCD signal with increasing Mn concentration is expected for the VB picture due to the Moss Burstein effect, whereas no shift is expected for the IB picture. Unfortunately both trends have been observed experimentally. A large background signal in MCD experiments, which has been attributed to transitions between the band states and the Mn_{Ga} impurity states [62], has been found to complicate the interpretation of the MCD results. These studies demonstrate the need for a better understanding of the electronic structure of GaMnAs. A logical direction would be to look for shifts in the linear absorption around the band gap to look for a Moss Burstein shift. The problem with this approach is that, due to low-temperature growth and Mn- and As-related disorder, a strong absorption tail dominates around E_g, preventing the extraction of a band gap energy [18].

Nonlinear techniques such as differential reflection and transmission, which provide a very different kind of optical probe than the linear experiments described above, and as such may be able to provide new insight into the open questions regarding the band structure of GaMnAs. These techniques also provide insight into the carrier dynamics in this system. Several differential reflection and transmission experiments have already been performed on GaMnAs [67, 68, 69, 70, 71, 72, 73, 74, 75, 76]. These experiments are performed either at a single probe energy, or over a narrow energy spectrum. This has led to considerable confusion with regard to the identification of different signal contributions, hindering the interpretation of the carrier dynamics.

As no spectrally-resolved experiments have yet been applied to this system in which a wide range of photon energies are used, no previous reported pump probe studies on GaMnAs have provided insight into the position of the Fermi level. In this thesis a broadband white light probe is used to study two GaMnAs samples and an LT-GaAs sample grown under similar conditions, as well a bulk GaAs sample. The results of these experiments have allowed the various contributions to the pump probe signal to be isolated. As discussed in Ch. 4, these experiments have also yielded new insight into the band structure and mechanism of ferromagnetic coupling in GaMnAs.

2.6 Signal Contributions to Pump Probe

In a pump-probe experiment a sample is hit first by a pump pulse which excites the sample, and at some time delay later is hit by a probe pulse which is used to monitor the associated pump-induced changes in the optical properties. In a differential transmission (reflection) experiment, the pump-induced change in transmission (reflection) is measured. For a direct band gap semiconductor containing defects, there are four potential contributions to the observed signal: (i) phase space filling, or state filling (PSF); (ii) free carrier absorption (FCA); (iii) defect-related absorption (DA); and (iv) band gap renormalization (BGR). These are described in more detail in the subsections below. These mechanisms are used to interpret the experimental results in this thesis, through calculations presented in Ch. 4.

2.6.1 Phase Space Filling

For a pump energy above the band gap of the semiconductor being excited, some of the pump photons will be absorbed and electrons will correspondingly be promoted from the valence band to the conduction band. Due to the Pauli exclusion principle, only two electrons (including spin) can occupy each allowed k state in the conduction band. As a result, the excitation process reduces the probability of absorption by additional photons at that photon energy, a phenomenon known as phase space filling (PSF). The associated pump-induced change in the optical response to the probe pulse is manifested in a differential transmission experiment as a positive signal (i.e. a reduction in absorption, often referred to as bleaching). In a differential reflection experiment, changes in both the absorption and index of refraction contribute to the

measured signal.

Excitation by the pump pulse leads to an initial distribution of electrons with a narrow range of energies in the conduction band, determined by the laser spectrum. Immediately after excitation, these carriers scatter with each other and redistribute in energy within the band, eventually forming an energy distribution that is well-described by the Fermi occupation function [77]. This distribution function is characterized by an elevated temperature (determined by the difference between the photon energy and the band gap energy) and an excited chemical potential [78]. As a result of the nonzero average occupation of the states in the conduction band, the probability of absorption at that photon energy by photons in the probe pulse is reduced. The non-equilibrium carrier density is given by

$$n = n_0 + n_{excited} = n_{intrinsic} \exp\left(\frac{\mu_{excited} - E_F}{k_B T}\right), \tag{2.1}$$

where n_0 is the equilibrium carrier density (obtained by integrating the product of the density of states and probability of occupation), $n_{excited}$ is the density of carriers excited by the pump, E_F is the Fermi energy in the absence of excitation, and $\mu_{excited}$ is the excited chemical potential. This can be rearranged to solve for the excited chemical potential,

$$\mu_{excited} = E_F + k_B T \ln \frac{n_{total}}{n_{intrinsic}}. \tag{2.2}$$

Once $\mu_{excited}$ is known, the thermalized population of electrons in the conduction band is given by the standard Fermi distribution $f(\omega)$ with the excited chemical potential substituted for the Fermi energy,

$$f_{excited}(\omega) = \left(\exp\left(\frac{\hbar\omega - \mu_{excited}}{k_B T}\right) + 1\right)^{-1}, \tag{2.3}$$

where ω is photon frequency. The density of states near the band edge of a semiconductor is given by [77],

$$DOS(\omega) = \frac{1}{2\pi^2}\left(\frac{2m_e}{\hbar^2}\right)^{\frac{3}{2}} \sqrt{\hbar\omega - E_g}, \tag{2.4}$$

where m_e is the effective electron mass and E_g is the band gap of the semiconductor.

The pump-induced reduction in available states, and thus the reduction is absorption coefficient is then given by [79]:

$$-\Delta\alpha_{PSF}(\omega) = f_{excited}(\omega) DOS(\omega). \tag{2.5}$$

This reduction in available states is known as phase space filling (PSF). The corresponding change in the index of refraction can be obtained by using the nonlinear Kramers-Krönig relations (KKR)[79]:

$$\Delta n(\omega) = \frac{c}{\pi}\text{P.V.}\int \frac{\Delta\alpha(\omega')}{\omega'^2 - \omega^2} d\omega', \tag{2.6}$$

where P.V. denotes Cauchy principal value. The reflectance of an absorbing medium perpendicular to the interface is given by

$$R(n(\omega), \kappa(\omega)) = \frac{(n(\omega) - 1)^2 + \kappa(\omega)^2}{(n(\omega) + 1)^2 + \kappa(\omega)^2}, \tag{2.7}$$

where n is the index of refraction and κ is the extinction coefficient. The extinction coefficient is related to the absorption coefficient by $\kappa = \frac{\alpha c}{2\omega}$. The pump-induced differential reflection is given by

$$DRR_{PSF}(\omega) = \frac{R(n_{PSF}(\omega), \kappa_{PSF}(\omega)) - R_0(n_0(\omega), \kappa + 0(\omega))}{R_0(n_0(\omega), \kappa_0(\omega))}, \tag{2.8}$$

where $n_0(\omega)$ is the unexcited index of refraction, $\kappa_0(\omega)$ is the unexcited extinction coefficient, R_0 is the unexcited reflectance, $n_{PSF}(\omega) = n_0(\omega) + \Delta n_{PSF}(\omega)$ and $\kappa_{PSF}(\omega) = \kappa_0(\omega) + \Delta\kappa_{PSF}(\omega)$. $\Delta n_{PSF}(\omega)$ and $\Delta\kappa_{PSF}(\omega)$ are the frequency dependent changes to the index of refraction and extinction coefficient caused by phase space filling.

2.6.2 Free Carrier Absorption

Upon excitation of the semiconductor by the pump pulse, electrons and holes are present in the band states. The associated carriers can respond to the probe pulse through intraband absorption, similar to the case of a metal. This contribution in a pump probe experiment is referred to as free carrier absorption (FCA). We can treat

this optical response of the material as a series of Lorentzian oscillators with a zero resonance frequency [80]. In this model, the real part of the dielectric constant is given by

$$\frac{\epsilon_R}{\epsilon_0} = 1 - \frac{\omega_p^2}{\omega^2 + \gamma^2}, \tag{2.9}$$

where γ is the transverse relaxation rate. The plasma frequency ω_p is given by

$$\omega_p = \sqrt{\frac{Ne^2}{m\epsilon_0}}, \tag{2.10}$$

where m is the effective electron mass, e is a single electron charge and N is the excited carrier density. The imaginary part of the dielectric constant is given by

$$\frac{\epsilon_I}{\epsilon_0} = \frac{\omega_p^2}{\omega^2 + \gamma^2}\frac{\gamma}{\omega}. \tag{2.11}$$

For free carriers injected by the pump, the pump induced change of index of refraction and coefficient of extinction can be calculated using

$$\Delta n_{FCA} = \sqrt{\frac{1}{2}\left(\frac{\epsilon_R}{\epsilon_0} + \sqrt{\frac{\epsilon_R}{\epsilon_0}^2 + \frac{\epsilon_I}{\epsilon_0}^2}\right)}, \tag{2.12}$$

$$\Delta \kappa_{FCA} = \sqrt{-\frac{1}{2}\left(\frac{\epsilon_R}{\epsilon_0} - \sqrt{\frac{\epsilon_R}{\epsilon_0}^2 + \frac{\epsilon_I}{\epsilon_0}^2}\right)}. \tag{2.13}$$

The overall index of refraction and coefficient of extinction are then given by $n_{FCA} = n_0 + \Delta n_{FCA}$, $\kappa_{FCA} = \kappa_0 + \Delta\kappa_{FCA}$, where Δn_{FCA} ($\Delta\kappa_{FCA}$) is the change in the index of refraction (extinction coefficient) in the presence of free carriers. The differential reflection signal due to carriers excited by the pump is given by

$$DRR_{FCA}(\omega) = \frac{R(n_{FCA}(\omega), \kappa_{FCA}(\omega)) - R_0(n_0(\omega), \kappa_0(\omega))}{R_0(n_0(\omega), \kappa_0(\omega))}. \tag{2.14}$$

2.6.3 Defect-Related Absorption

Once carriers have been excited from the valence to the conduction band, they can get trapped in deep midgap trap states. Once trapped in midgap states, these carriers

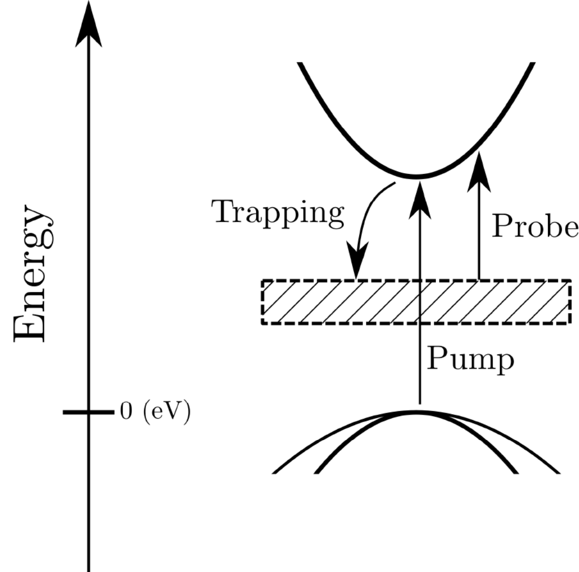

Figure 2.7: Schematic diagram of defect-related absorption processes in a direct band gap semiconductor. After inital excitation by the pump, excited carriers get trapped to defect states where they can be re-excited by the probe to the conduction band.

can be excited by the probe to states higher in the conduction band, leading to pump-induced absorption. Since the trapped midgap states are due to As defects, which occur in an aperiodic manner, conservation of momentum is relaxed and these carriers can be excited to any state in the conduction band provided there is sufficient probe photon energy to do so. Transitions from the valence band to midgap states are ignored because the absorption cross section of these transitions are roughly an order of magnitude lower than those from mid-gap states to the conduction band [43]. A schematic diagram is shown in Fig. 2.7. The extra absorption induced by the pump pulse through this process may be described using

$$\Delta\alpha_{DA}(\omega) = A \cdot DOS(\omega), \tag{2.15}$$

where $\Delta\alpha_{DA}(\omega)$ is the additional absorption caused by the trapped carriers, A is a proportionality constant and $DOS(\omega)$ is given by Eqn. 2.4 with E_g replaced by $E_g/2$. Equation 2.4 is inspired by the experimental data in [43]. The numerical value of A will be determined by the density of trapping defects and the number density of trapped carriers following optical excitation. As these quantities may not be determined in practice, the value of A is used as a fitting parameter in interpreting

the experimental results. The change in the index of refraction can be calculated using the nonlinear Kramers-Krönig relations (Eqn. 2.6). The differential reflectivity due to defect-induced absorption (DA) can then be calculated using

$$DRR_{DA}(\omega) = \frac{R(n_{DA}(\omega), \kappa_{DA}(\omega)) - R(n(\omega), \kappa(\omega))}{R_0(n_0(\omega), \kappa 0(\omega))}, \tag{2.16}$$

where n_{DA} (κ_{DA}) are the sum of n_0 (κ_0) and Δn_{DA} ($\Delta\kappa_{DA}$) respectively. Δn_{DA} and $\Delta\kappa_{DA}$ are the defect-related changes in index of refraction and extinction coefficient, respectively.

2.6.4 Band Gap Renormalization

Band gap renormalization (BGR) is a many-body effect which occurs in an interacting electron gas. When many carriers are excited to the conduction band by the pump, the reduced Coulomb repulsion resulting from the Pauli exclusion principle results in a negative exchange self energy. This self-energy increases in magnitude with increasing carrier concentration. The free-particle energy is modified by the exchange self energy, resulting in a reduction in the band gap [81]. Such a pump-induced shift of the band gap will produce a change in the absorption and index of refraction for states near the band gap. This results in a pump-probe signal.

For a pump-induced bandgap shift of ΔE_g the change in absorption will be given by

$$\Delta\alpha_{BGR}(E, \Delta E_g) = \alpha(E + \Delta E_g) - \alpha(E). \tag{2.17}$$

The corresponding change in index of refraction is then given by

$$\Delta n_{BGR}(\omega, \Delta E_g) = \frac{c}{\pi}\text{P.V.}\int \frac{\alpha(E_g + \Delta E_g) - \alpha(E_g)}{\omega'^2 - \omega^2} d\omega'. \tag{2.18}$$

The differential reflectivity due to BGR can be calculated using

$$DRR_{BGR}(\omega, \Delta E_g) = \frac{R(n_{BGR}(\omega, \Delta E_g), \kappa_{BGR}(\omega, \Delta E_g)) - R_0(n_0(\omega), \kappa_0(\omega))}{R_0(n_0(\omega), \kappa_0(\omega))}, \tag{2.19}$$

where n_{BGR} (κ_{BGR}) are the sum of n_0 (κ_0) and Δn_{BGR} ($\Delta\kappa_{BGR}$) respectively. Δn_{BGR} and $\Delta\kappa_{BGR}$ are the BGR-induced changes in the index of refraction and coefficient

of extinction, respectively.

Determination of the magnitude of the band gap shift associated with BGR is a complicated theoretical task, especially for materials with a large defect concentration. In this thesis, the size of the band gap shift will be taken from experiments performed in HT-GaAs [4].

2.6.5 Sample Pump Probe Results: High Temperature Grown Undoped GaAs

An example of experimental data that illustrate some of these effects is shown in Fig. 2.8. Lee et al. [4] measured absorption spectra of bulk GaAs in an experiment where a 1.51 eV beam of varying intensity was used to pump the sample and a broadband CW probe was used to measure the pump-induced change in the absorption spectrum. A reduction in absorption was observed over a broad range of energies, and the reduction increased with increasing probe intensity. These experiments, together with the associated theoretical analysis, allowed the authors of Ref. [4] to conclude that state filling provides the dominant contribution to the nonlinear optical response of bulk GaAs.

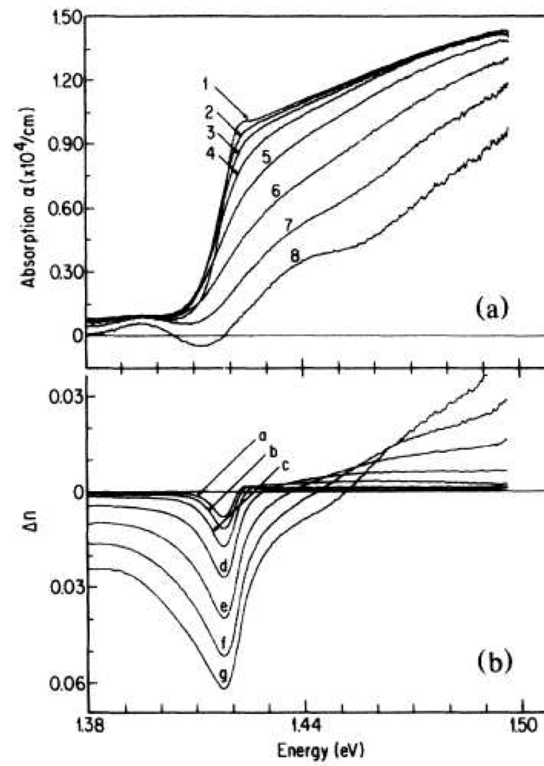

Figure 2.8: (a) Room temperature absorption spectra of bulk GaAs with excitation powers between 0 and 50 mW on a 15 μm spot size. (b) Δn extracted from data in (a) via nonlinear KKR [4].

Chapter 3

Overview of Experiments

3.1 Chapter Outline

This chapter contains a description of the samples studied (Sec. 3.2) as well as the experimental technique (Sec. 3.3) and equipment (Sec. 3.4) used to study them. The method used for calculating the density of carriers excited by the pump beam is given in Sec. 3.5.

3.2 Samples

Four samples were studied in this thesis, as shown in Table 3.1. Three of the samples (G030-3, F066-6 and G114) were grown by molecular beam epitaxy by Vit Novak at the Institute of Physics at the Academy of Sciences of the Czech Republic. The research group of Vit Novak is world renowned for growth and materials engineering of GaMnAs [20, 82, 6, 83]. A fourth sample consisting of a semi-insulating GaAs substrate was purchased from Wafer Technology Ltd.

For differential reflectivity experiments, one would like to have the layer under study be optically thick (i.e. to have a thickness two times greater than the absorption depth) in order to avoid a pump probe response from the substrate and buffer layers. Obtaining a high T_C in GaMnAs requires post-growth annealing, which has the effect of removing Mn_i defects, producing the largest possible fraction of Mn atoms in substitutional sites and thereby the largest concentration of holes. This annealing

Sample	T_{growth}	x (%)	T_C	Thickness (nm)
SI GaAs	HT	0	N/A	N/A
G114	LT	0	N/A	150
G030-3	LT	10	115-135	150
F066-3	LT	12	183	21.5

Table 3.1: Summary of physical characteristics of samples studied.

process is more effective the thinner the GaMnAs epilayer, since Mn interstitials can diffuse to the surface more easily in that case [84]. A compromise for this study was taken with an epilayer of 150 nm thickness. In order to assess the influence of the substrate on the observed differential refection results, a thinner GaMnAs sample (20.5 nm) was also studied for comparison. The pump probe response of a reference LT-GaAs samples (also 150 nm thick) as well as a plain GaAs sample was also measured for comparison with the GaMnAs samples.

3.3 Pump Probe Spectroscopy

Pump probe spectroscopy is an experimental technique which can be used to study time-resolved changes in the optical properties of materials. A pulse train from a pulsed laser source is split into two beams, and these pulse trains are then directed onto the sample of interest. The more powerful of the two pulse trains is called the pump beam, and the weaker pulse train is called the probe beam. The probe is used to detect pump-induced changes in the optical characteristics of the sample (e.g. reflection or transmission). The time evolution of the pump-induced probe response is monitored by changing the delay between the pump and probe pulses using a mechanical delay line. A basic diagram of the experimental arrangement is shown in Fig. 3.1. A ratio of pump power to probe power of approximately 10:1 was used in this experiment. Since the duration of the pump and probe pulses is on the order of 100 fs, very short timescales can be resolved and the field of study which exploits this technique is called *ultrafast spectroscopy*. If the pump and probe pulses have different photon energies, the experiment is called a non-degenerate pump-probe experiment.

The most intuitive pump-probe experiment to consider is the case of a degenerate differential transmission experiment, in which the component of the probe that is transmitted through the sample is measured. In this case, carriers excited by the pump pulse will temporarily increase the chemical potential by promoting electrons to the conduction band, reducing the absorption coefficient due to state filling. The reduction in absorption will result in a corresponding increase in the fraction of the probe which is transmitted. In this case the quantity of interest is the change in transmittance ΔT, which is typically normalized to the unsaturated transmittance T_0, so that $\left(\frac{\Delta T}{T_0}\right)$ is presented. The change in transmission ΔT can be measured with

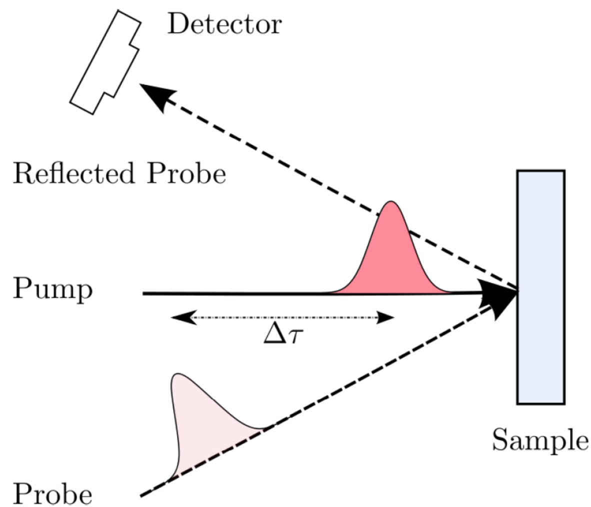

Figure 3.1: Schematic diagram of pump probe spectroscopy, shown in the differential reflection geometry. The time interval $\Delta\tau$ between the pump and probe pulses on the sample can be controlled by varying the optical path length of the probe with respect to the pump.

a lock-in amplifier by modulating the pump pulse train with an optical chopper, and monitoring the voltage signal from the probe detector. The unsaturated transmission T_0 is then measured by modulating the probe pulse train. In the case of differential reflection, interpreting the signal is slightly more complicated because changes in both the absorption and index of refraction affect the signal, as discussed in Ch. 2.

3.4 Experimental Apparatus

The laser source for these experiments is shown in Fig. 3.2. The Verdi V-18 has a gain medium of Neodymium-doped yttrium orthovanadate ($Nd:YVO_4$), which has a lasing wavelength of 1064 nm. This is upconverted to 532 nm via second harmonic generation in a Lithium triborate (LBO) crystal yielding the final output of the Verdi. The Verdi optically pumps the Mira-SEED laser and the RegA 9050. The Mira-SEED is a 76 MHz mode-locked ultrafast laser which produces ultrashort femtosecond pulses using Titanium:sapphire as a gain medium. The output is tunable from 780 to 840 nm. In this experiment 800 nm was used as the centre wavelength of the output with a bandwidth (full width half maximum) of 30 nm. The output is directed to a pulse stretcher which stretches out the pulses in time by introducing group velocity dispersion (GVD) through four passes off a grating. The pulses are stretched to avoid

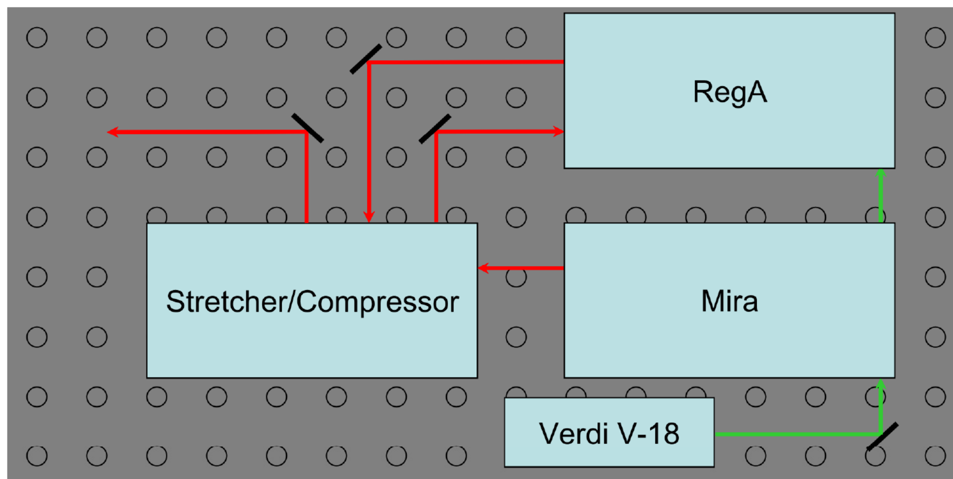

Figure 3.2: Layout of the laser system on the optical table.

damage to optical elements when these pulses are amplified.

The RegA is a Ti:sapphire regenerative amplifier which takes a pulse from the pulse stretcher, amplifies it by repeatedly sending it through a gain medium and then ejects the pulse. The repetition rate of the RegA is 250 KHz. The amplified pulse is then sent to the compressor where the GVD introduced by the stretcher is removed. The output from the compressor is then sent to a beam splitter. One of the outputs of the beam splitter becomes the pump and the other is directed to a sapphire crystal which is used to generate a white light continuum, which becomes the probe.

Once the pump and probe are generated they are sent into the experimental apparatus used to perform the pump probe experiments. A schematic diagram of this apparatus is shown in Fig. 3.3. The path length of the pump beam (shown in green), is varied by a retroreflector mounted on an externally-controlled mechanical delay stage. The delay stage has a resolution of 0.2 μm which corresponds to a time resolution of 1.3 fs. Comparing this to the 150 fs pump duration shows that the delay stage is not the limiting factor in experimental time resolution. The probe, represented by the red path, is directed along a fixed length path. A half wave plate is placed in the probe path which rotates the polarization of the probe by 90° so that the pump and probe are cross-polarized. Both beams are focused onto the sample with achromatic lenses with a focal length of 25 mm. The sample is mounted on the same focal plane as a 50 μm pinhole, and both are accessible to the laser through quartz windows. The cryostat and the lenses are mounted on independent 3D stages. Spatial overlap

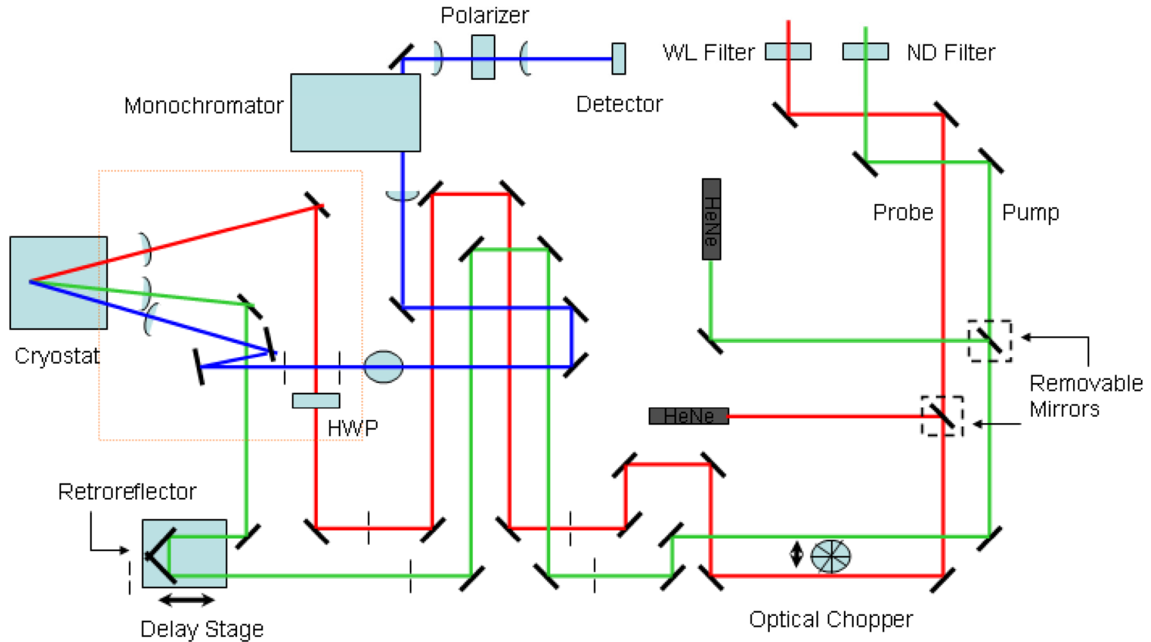

Figure 3.3: Schematic of the experimental apparatus. The green path represents the pump, the red path the probe and the blue the post-sample reflected probe.

of the pump and probe beams is achieved by first optimizing the probe transmission through the pinhole by adjusting the cryostat position and then optimizing the pump transmission through the pinhole by adjusting the pump focusing lens. The reflected probe beam is recollimated with another 25 mm achromatic lens and directed through a monochromator and polarizing cube followed by a variable gain photodiode detector. The polarizer is used to reject scattered pump light from the sample.

Before any data is collected the cryostat is evacuated by the rotary pump. Pressures below 10^{-2} Torr are sufficient to perform experiments at liquid nitrogen temperature without condensation building up on the cryostat. Once the cryostat is evacuated, it is cooled with liquid nitrogen. The sample is heated to 80 K by Joule heating using a loop of wire controlled by a PID loop on a temperature controller. An integrated diode is used to measure the temperature. Once overlap has been achieved the cryostat is raised so that the beams are incident on the sample. The pump induced change in the probe reflectivity is detected by modulating the pump beam using an optical chopper and monitoring the probe detector signal using a lock-in amplifier to lock in on the chopper frequency. The overlap of pump and probe is further optimized by

moving the delay stage to a fixed post-pump delay and maximizing the ΔR signal by adjusting the pump lens.

The optical response to the reflected probe beam in the absence of the pump beam (R_0) is also measured with the lock-in amplifier by blocking the pump and moving the optical chopper into the probe beam. $\left(\frac{\Delta R}{R_0}\right)$ scans are taken at a given wavelength by measuring R_0 and then measuring ΔR as a function of delay using a LabView program that controls the position of the delay stage.

3.5 Laser Spot Size and Excitation Density

The spot size of the laser beam on the sample is determined by measuring the transmission of the beam through the same pinhole that is used for spatial overlap. The spot size is given by

$$w = \sqrt{\frac{-2}{ln\,(1 - PT)}}a, \tag{3.1}$$

where w is spot radius, PT is the ratio of transmitted to incident power on the pinhole, and a is the pinhole radius. Measuring the power before and after the pinhole yields a spot size of 28.3 μm.

The excited carrier density is given by

$$n_{excited} = \frac{\text{\# of photons per pulse} \times \text{Fraction of light absorbed}}{\text{Volume excited}}. \tag{3.2}$$

In this experiment for a typical pump power of 8.91 mW, the excited carrier density for a 150 nm GaAs sample is $3.99 \times 10^{19}\text{cm}^{-3}$. Details of this calculation are shown in Appendix A.

Chapter 4

Results and Discussion

4.1 Chapter Outline

This chapter begins with a presentation of the experimental results in Sec. 4.2, consisting of spectrally-resolved differential reflectivity studies on GaMnAs, GaAs and LT-GaAs. The results of theoretical calculations of the pump probe signals are presented in Sec. 4.3. A discussion of the thesis results in the context of the present understanding of the electronic structure of GaMnAs is presented in Sec. 4.4.

4.2 Spectrally-Resolved Differential Reflectivity Experiments in GaMnAs

The optical response of SI GaAs provides a useful benchmark for the studies of GaMnAs in this thesis because the carrier dynamics in SI GaAs have been well characterized in past work [4, 85, 86, 87]. The salient features of the measured differential reflectivity response of SI GaAs are apparent from the data in Fig. 4.1. For all data in this thesis, the sample temperature is 80 K, the centre photon energy of the pump pulse is 1.55 eV, and the excited density of electron-hole pairs is $3.99 \times 10^{19}\text{cm}^{-3}$. For the data in Fig. 4.1, the probe photon energy is 1.652 eV, providing a measurement of the change in the optical response above E_g caused by the pump-injected carriers. Following excitation by the pump pulse, the carriers undergo a cascade of processes before they ultimately recombine [88]. Immediately following excitation, the carriers form a nonthermal distribution, with an energy spectrum dictated by the laser spectrum. During the first few hundred femtoseconds, carriers scatter with each other, leading to a redistribution within the band states until they form a Fermi distribution characterized by a nonequilibrium chemical potential and temperature. The initial temperature of the electron distribution is dictated by the excess energy of the pump photons (42 meV of excess energy corresponds to an average electron temperature of

330 K), and the chemical potential is dictated by the pump pulse fluence (i.e. the optically-injected carrier density). The thermalised, hot carrier distribution subsequently cools through the emission of phonons until the temperature of the carrier distribution equals the lattice temperature (80 K). On a much longer time scale, the carriers recombine. In the data of Fig. 4.1, the initial spike is likely due to a coherent artifact (a coherent coupling effect between the pump and probe beams which leads to a spurious signal during pulse overlap) [89]. The dynamics of the optically-injected carriers are reflected by the evolution of the differential reflectivity signal versus time delay following this initial spike. As seen in Fig. 4.1, the differential reflectivity signal initially increases as the carrier distribution thermalises. This reflects the fact that the hot carriers occupy states over a range of energies, leading to the creation of a state filling response above E_g. This signal then decays as the carriers cool to the lattice temperature, since the lower the temperature of the carrier Fermi distribution, the smaller the state filling response at a given photon energy above E_g. This cooling process causes the signal at 1.652 eV to decay to almost zero in the first 50 ps. The small residual signal (caused by the small tail of the cold Fermi distribution) decays on a much longer time scale as the carriers recombine. The electron-hole recombination time is longer than the total range of optical delays in the experimental apparatus used here, and so state filling persists throughout the accessible range of delays (up to $\sim$ 2 ns).

It is clear from the above discussion that a more comprehensive view of the carrier dynamics may be obtained from measurements of the differential reflectivity response over a range of probe energies. The results of spectrally-resolved differential reflectivity experiments on SI-GaAs are shown in Fig. 4.2 The differential reflectivity signal for early time delays is shown in Fig. 4.2(a), and for longer time delays in Fig. 4.2(b). The state filling signal is indicated in Fig. 4.2 by the positive (red) signal above the band gap of GaAs (1.507 at 80 K). Induced absorption associated with the Drude response of the pump-injected carriers (i.e. FCA, as described in Sec. 2.6.2) leads to a negative (blue) differential reflectivity signal, which dominates below E_g where the state filling signal is absent. The process of carrier cooling is evident in the data in Fig. 4.2(a) by the convergence of the state filling signal to a spectrally-narrow response just above E_g within the first 40-50 ps. Carrier recombination causes a slow

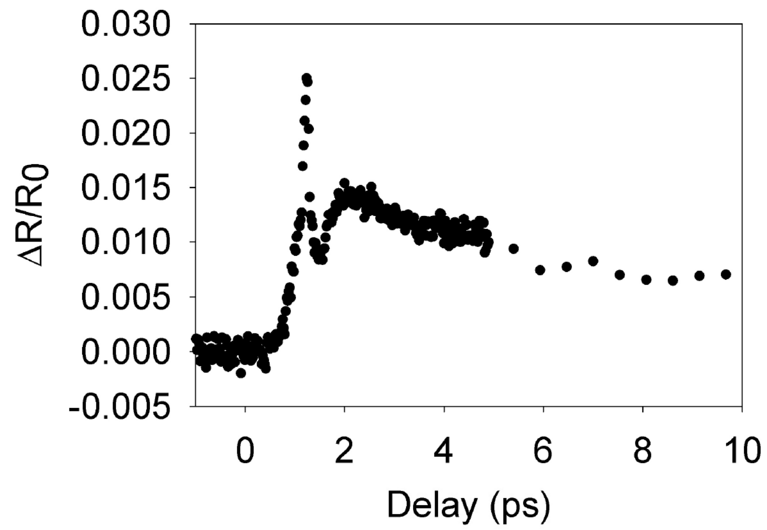

(a)

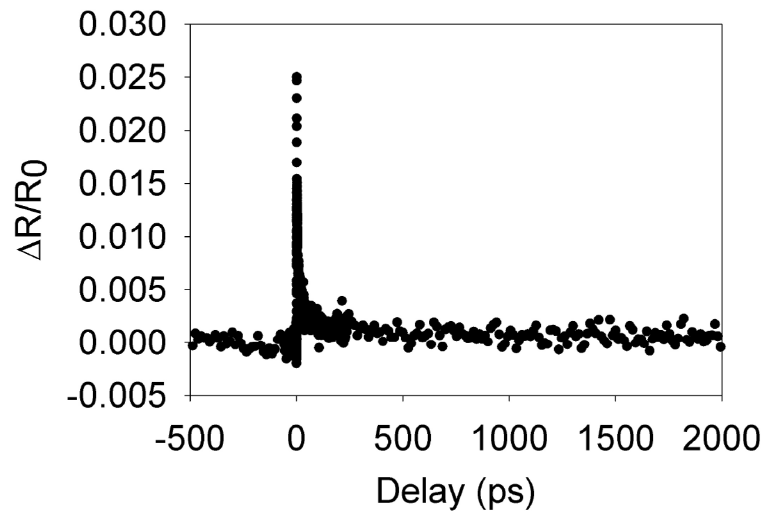

(b)

Figure 4.1: Differential reflection of SI GaAs at probe energy 1.652 eV at (a) short delays and (b) long delays.

decay of the state filling response between 50 ps and 2 ns. These results are similar to those observed previously in undoped GaAs [4, 85, 86, 87].

The carrier dynamics are expected to be quite different in GaMnAs than in SI-GaAs because low-temperature growth leads to the presence of a large density of As_{Ga} defects, as discussed in Ch. 2. These defects represent strong trapping sites for electrons. The carrier trapping dynamics have been studied extensively in LT-GaAs and LT-InP [39, 90, 91, 92, 93]. Electrons that have become trapped can be promoted by the probe photons to states high in the conduction band, creating a DA signal, as discussed in Sec. 2.6.3. The results of differential reflectivity experiments on sample G030-3 (referred to in this chapter as the 150 nm GaMnAs sample) are presented in Fig. 4.3. These data correspond to the same probe photon energy as in Fig. 4.1. In contrast to the results for the SI-GaAs sample in Fig. 4.1, the differential reflectivity response in the 150 nm GaMnAs sample exhibits a large negative signal on short time scales. This signal subsequently changes sign, producing a positive signal for longer delays, which persists to the end of the measurement range. Since the sign of the coherent artifact signal should be the same in both SI-GaAs and GaMnAs [89], the large negative signal for early time delays in Fig.4.3 must reflect the optical response of the carriers. This negative signal is attributed to free carrier absorption, which is enhanced in the presence of defects due to the partial relaxation of the wavevector conservation rule for optical transitions [18, 72, 69, 92, 94]. The decay of the negative signal is caused by trapping of carriers by the As_{Ga} defects. Fitting the exponential rise in Fig. 4.3(a) yields an estimate for the electron trapping time of 2 ps, in agreement with measured trapping times in LT-GaAs and LT-InP by other groups, which is in the range of a few hundred femtoseconds to 1.6 ps [90, 39, 91]. The positive signal for larger delay times is attributed to a DA signal associated with the trapped carriers. This DA signal at long delays is absent in SI-GaAs because it is grown at high temperatures and therefore has a negligible density of As_{Ga} defects compared to the low-temperature-grown samples.

The results of spectrally-resolved differential reflectivity measurements on the 150 nm GaMnAs sample are shown in Fig. 4.4. The most notable difference between the spectrally resolved data in Fig. 4.4 and Fig. 4.2 is that the signal in GaMnAs exhibits a strong, spectrally-broad response at high photon energies. As discussed above, we

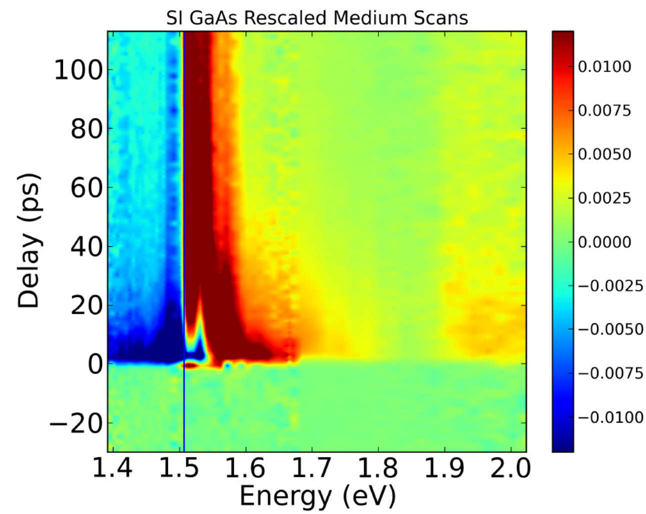

(a)

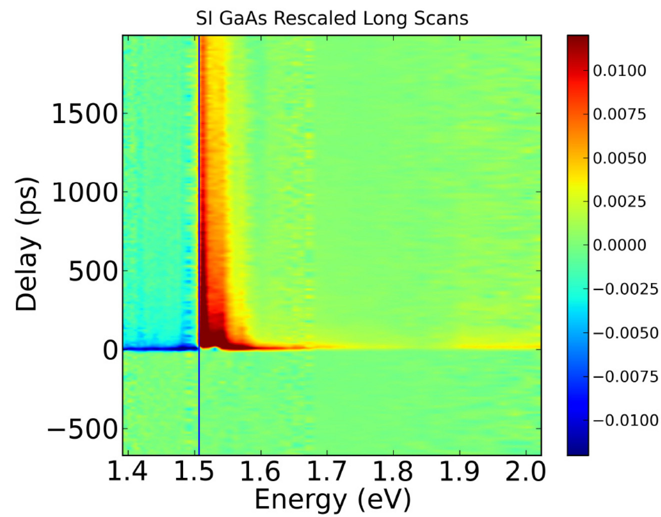

(b)

Figure 4.2: Differential reflection of the SI GaAs sample. Probe energy is shown in the horizontal axis while delay is shown on the vertical axis for (a) short delays and (b) for long delays. The colour corresponds to the DRR signal level at a given energy and delay. The band gap of GaAs at 80 K is indicated with a blue line. The fast dynamics at early time scales are not captured in these 3D plots due to the finite mesh used to generate the plot.

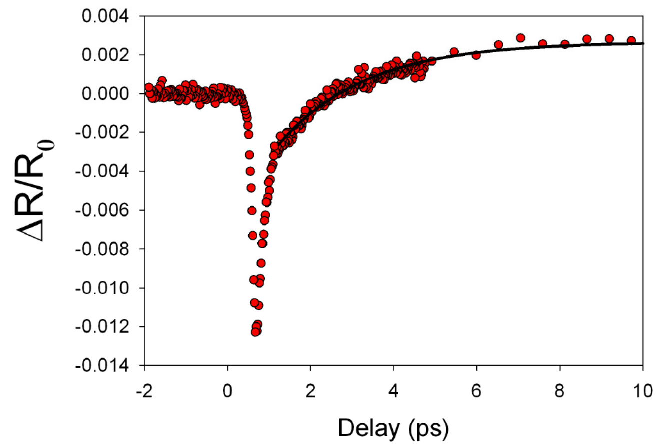

(a)

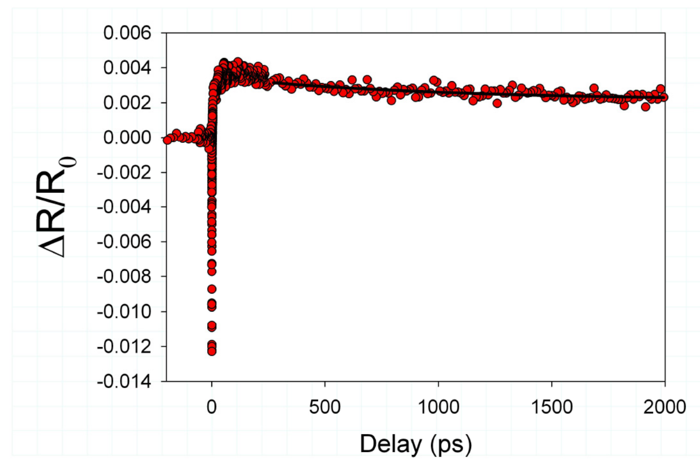

(b)

Figure 4.3: Differential reflection of 150 nm thick GaMnAs at probe energy 1.652 eV at (a) short delays and (b) long delays.

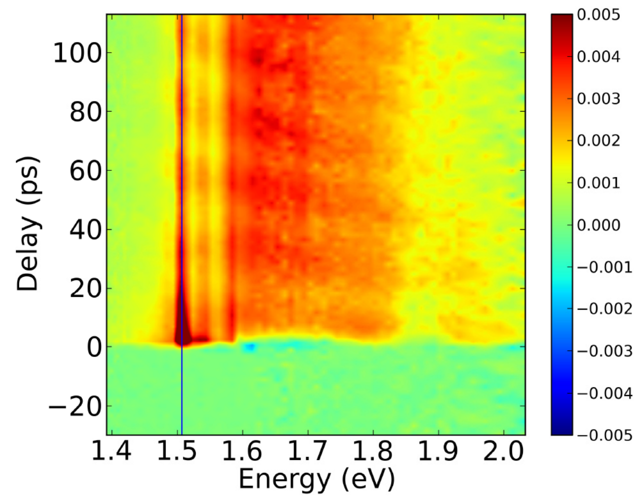

(a)

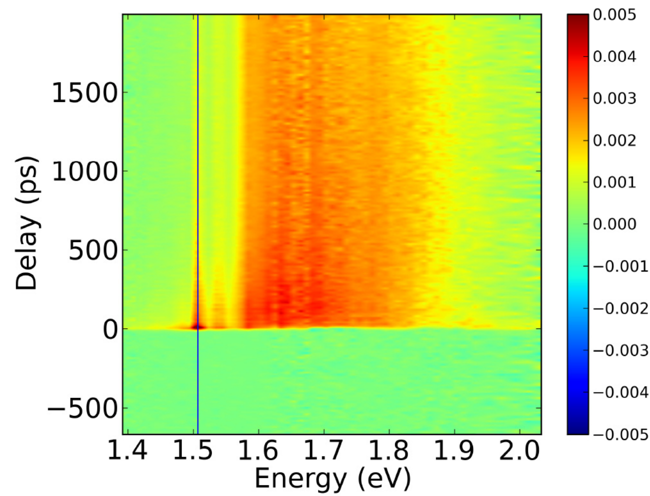

(b)

Figure 4.4: Differential reflection of the G030-3 GaMnAs sample. Probe energy is shown in the horizontal axis while delay is shown on the vertical axis for (a) short delays and (b) for long delays. The colour corresponds to the DRR signal level at a given energy and delay. The band gap of GaAs at 80 K is indicated with a blue line. The fast dynamics at early time scales are not captured in these 3D plots due to the finite mesh used to generate the plot.

attribute this positive signal to DA associated with trapped carriers. Such a response is expected to be spectrally-broad as conservation of momentum is not required in the excitation process from the As_{Ga} donor band to the conduction band. This interpretation is supported by differential reflectivity results in sample G114 (LT-GaAs) in Fig. 4.5, which also exhibits a spectrally-broad response. The DA signal in the data for LT-GaAs is observed to decay faster than the DA signal in the 150 nm GaMnAs sample. The defect distribution is expected to vary to some extent from sample to sample, as all of the low-temperature-grown samples studied in this thesis work were grown at different times and under slightly different conditions. These variations are expected to lead to small differences in the nature of the DA response. For example, a different degree of compensation will modify the initial density of trapping sites, affecting the overall magnitude of the DA response [95]. Variation in the level of disorder will also modify the density of states high in the conduction band [18], which could lead to variations in the shape of the DA signal for large photon energies. The faster decay of the DA signal in LT-GaAs compared to the 150 nm GaMnAs sample implies that carriers recombine from the trap states at a higher rate in the LT-GaAs sample. A variety of mechanisms for recombination have been suggested in studies of carrier dynamics in LT-GaAs [39, 90, 91, 92, 93] (*e.g.* Lochetfeld et al. attributed the long-lived signal to the recombination of trapped electrons with delocalized holes[90]). It is reasonable to expect this recombination time to vary with the details of the defect distribution, in agreement with the measured results.

Another notable difference between the results in Fig. 4.2 and Fig. 4.4 is that the sharp onset of signal in the SI-GaAs occurs at 1.507 eV (the band gap of GaAs at 80 K), while in GaMnAs it occurs at higher energies (approximately 1.57 eV). This shift is attributed to the influence of the Mn doping, and is discussed further in Sec. 4.3. In the data in Fig. 4.4, a weak feature also appears at 1.507 eV. This feature is attributed to the optical response of the GaAs buffer layer, which is grown at high temperatures and so should exhibit a carrier response similar to the results in Fig. 4.2 for SI-GaAs. This was verified through comparison of the measured results in the 150 nm GaMnAs sample to corresponding measurements in a thinner (20 nm) GaMnAs sample (F066-3), for which the data is shown in Fig. 4.6. The GaAs buffer layer will influence the observed signal characteristics for photon energies for which

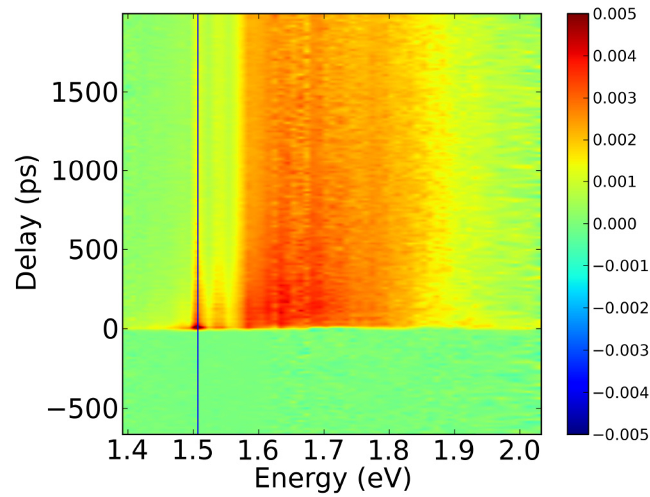

(a)

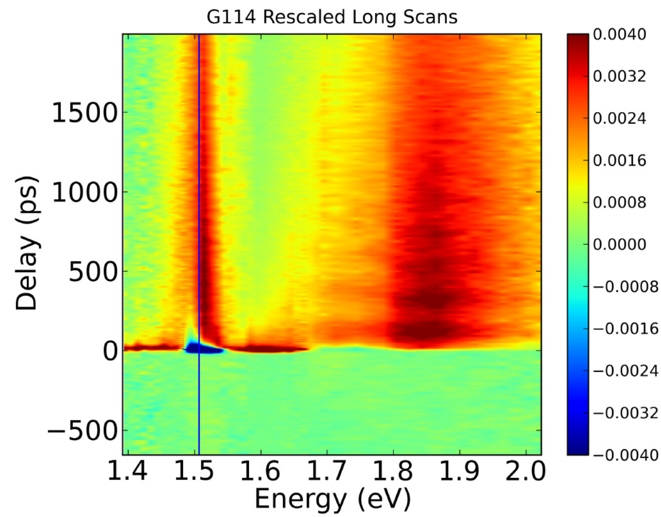

(b)

Figure 4.5: Differential reflection of the (a) 150 nm GaMnAs sample and (b) LT GaAs sample. Probe energy is shown in the horizontal axis while delay is shown on the vertical axis. The colour corresponds to the DRR signal level at a given energy and delay. The band gap of GaAs at 80 K is indicated with a blue line. The fast dynamics at early time scales are not captured in these 3D plots due to the finite mesh used to generate the plot.

the absorption depth exceeds two times the thickness of the GaMnAs layer. The larger response at 1.508 eV in the 20 nm sample than in the 150 nm sample indicates that this feature is associated with a state-filling signal in the buffer layer. Aside from this buffer layer response, the qualitative features in the 20 nm GaMnAs sample are similar to those in the 150 nm GaMnAs sample, including the observation of a broad signal response associated with DA and the blue shift in the onset of the optical response relative to the band gap of GaAs. Since these two samples were grown at different times and under slightly different conditions, these general trends are considered to be global properties of the optical response of GaMnAs.

We note that there is an additional weak, spectrally-narrow feature in the results for the 150 nm thick sample around the pump photon energy (1.55 eV). The origin of this weak feature, which is not present in any of the other samples, is not known. Pronounced oscillations are also observed in the data for the low-temperature grown samples. These were seen in earlier studies of carrier dynamics in GaMnAs [96] and InMnAs [97], and are attributed to the excitation of coherent phonons in the surface layer of the sample, which modifies the index of refraction. As this phonon wavepacket propagates into the sample, interference associated with the reflection from this moving layer causes delay-dependent oscillations.

4.3 Calculated Differential Reflection Signals

In order to gain more insight into the experimental results in Sec. 4.1, numerical simulations were performed using an approximate model for each of the physical mechanisms that can contribute to the pump probe signals in these samples. The mechanisms considered are state filling, free carrier absorption, band gap renormalization and defect induced absorption (which have already been introduced in Sec. 2.6). The pump-induced changes in index of refraction, extinction coefficient and differential reflection for each of these signal contributions have been calculated and are shown in Fig. 4.7. For the bandfilling, DA and BGR signals, the change in index of refraction was calculated from a change in absorption coefficient that was defined analytically as discussed in Sec. 2.6 using the nonlinear Kramers-Krönig transformation. This calculation involves an integral over the entire frequency range of the change in absorption. This integral could be performed accurately as the analytic model of the

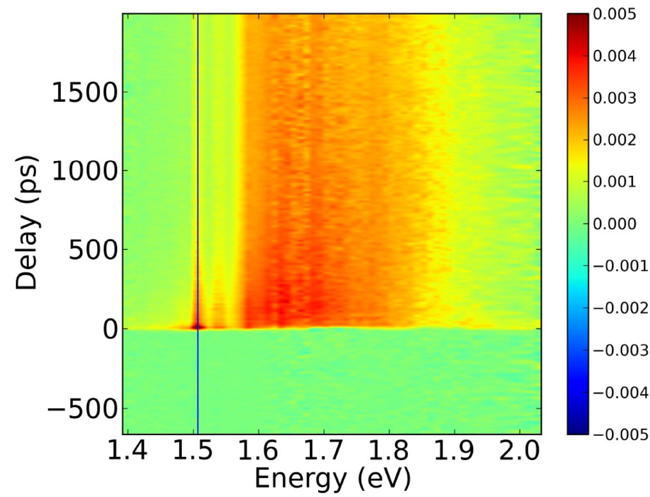

(a)

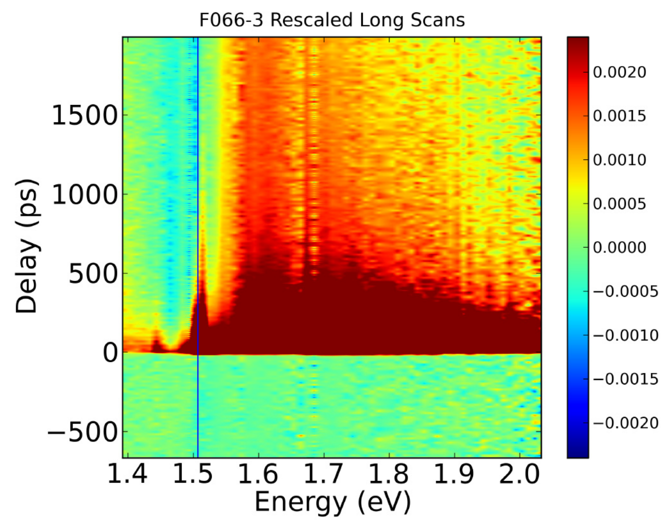

(b)

Figure 4.6: Differential reflection of the (a) 150 nm GaMnAs sample and (b) 20 nm GaMnAs sample. Probe energy is shown in the horizontal axis while delay is shown on the vertical axis. The colour corresponds to the DRR signal level at a given energy and delay. The band gap of GaAs at 80 K is indicated with a blue line. The fast dynamics at early time scales are not captured in these 3D plots due to the finite mesh used to generate the plot.

change in absorption is known for all frequencies. The Cauchy principal value of the integral was computed by integrating up to discontinuities in the integrand to within a certain interval ϵ. ϵ was chosen to be sufficiently small that the calculated change in index of refraction would remain constant as ϵ was further decreased. The upper limit of integration was chosen to be ≥ 1000 times the band gap energy. Further extending the integration range did not change the result of the calculation.

For these calculations, the unsaturated reflectivity (R_0) was obtained using Eqn. 2.7. For this calculation, the unsaturated index of refraction (n_0) was obtained from the measured dependence of the real part of the dielectric function on photon energy in GaAs reported in Ref. [18], which was shifted by the difference in band gap between 300 K and 80 K to approximate the unsaturated index of refraction at the experimental temperature. The unsaturated absorption coefficient (α_0) was modeled by scaling the density of states in Eqn. 2.4 so that it matched the experimental absorption of GaAs at 77 K 100 meV above band gap as measured by M. D. Sturge [98]. The resulting R_0 values were used for all calculations.

As discussed in Ch. 2, state filling is caused by the optically excited carriers, which change the chemical potential. The carrier density in the experiment was determined as described in Sec. 3.5 to be $3.99 \times 10^{19}\text{cm}^{-3}$. In this case it was verified that the chemical potential is well described by Eqn. 2.2, as we are in the nondegenerate limit [78]. As shown in Fig. 4.7 (a, b), the state filling leads to a sharp change in the extinction coefficient and a sharp feature in the change of index of refraction near the band gap. These sharp features lead to sharp features in the calculated bandfilling $\frac{\Delta R}{R_0}$ signal (shown in Fig. 4.7 (c)). The sharpness of the features in the extinction coefficient, index of refraction and differential reflection is due to the model containing a square root function for the density of states. In reality, the density of states would have a smoother edge as bandtailing and excitonic effects are neglected. Further, the square root density of states is only valid within a few hundred meV of the band edge after which the effective mass approximation begins to break down. The calculated state filling signal at the experimental carrier density is shown in Fig. 4.8 (a) with the solid line.

The optical signal associated with FCA was also calculated numerically. The dominant contribution to FCA is due to the electrons, which have a smaller effective mass

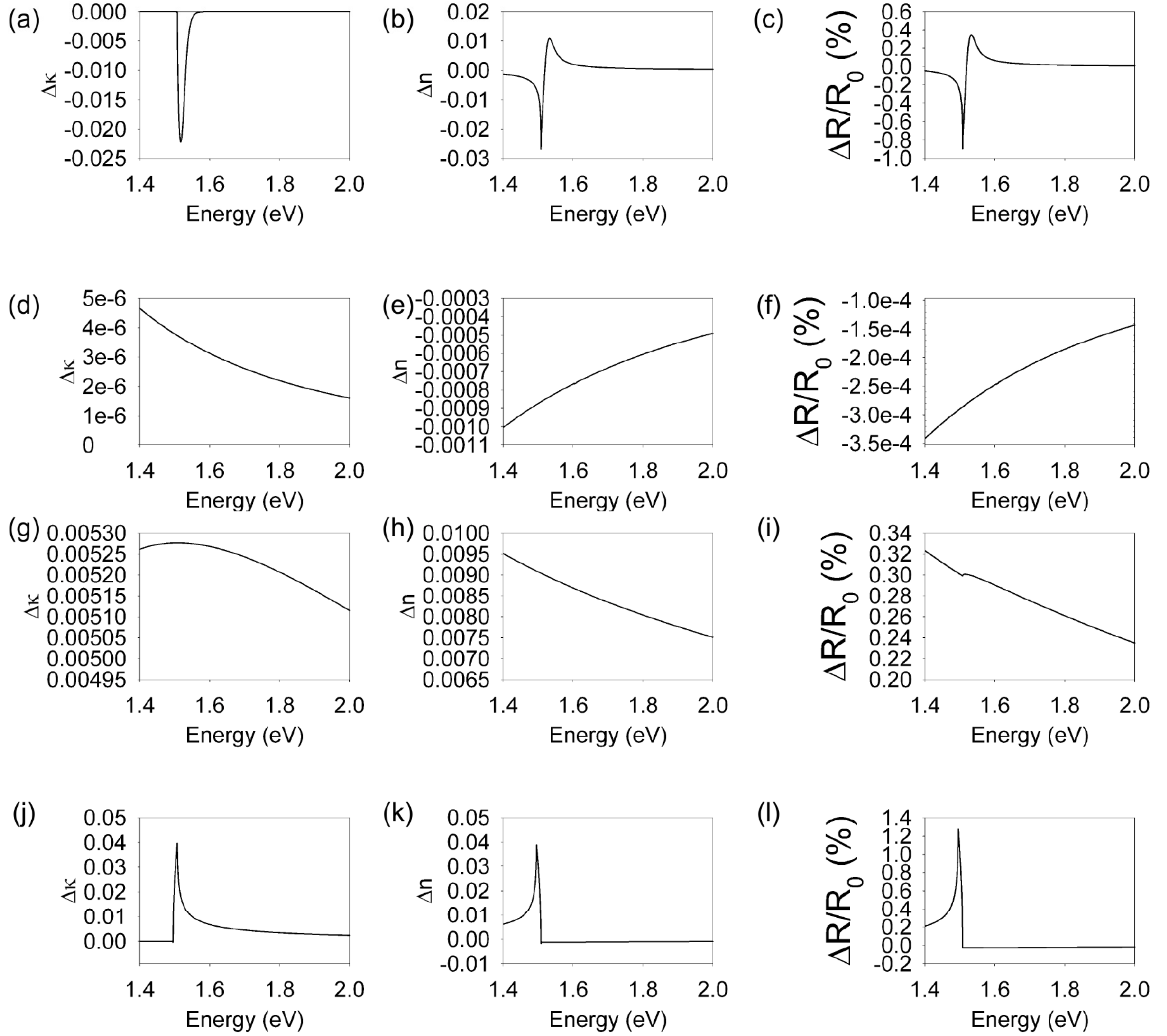

Figure 4.7: Calculated pump-induced changes in the extinction coefficient, index of refraction and differential reflection are shown for various signal contributions in the first, second and third columns respectively. Changes due to bandfilling, FCA, DA and BGR are shown in the first through fourth rows respectively. A carrier density of $2 \times 10^{18}\text{cm}^{-3}$ was used in these calculations.

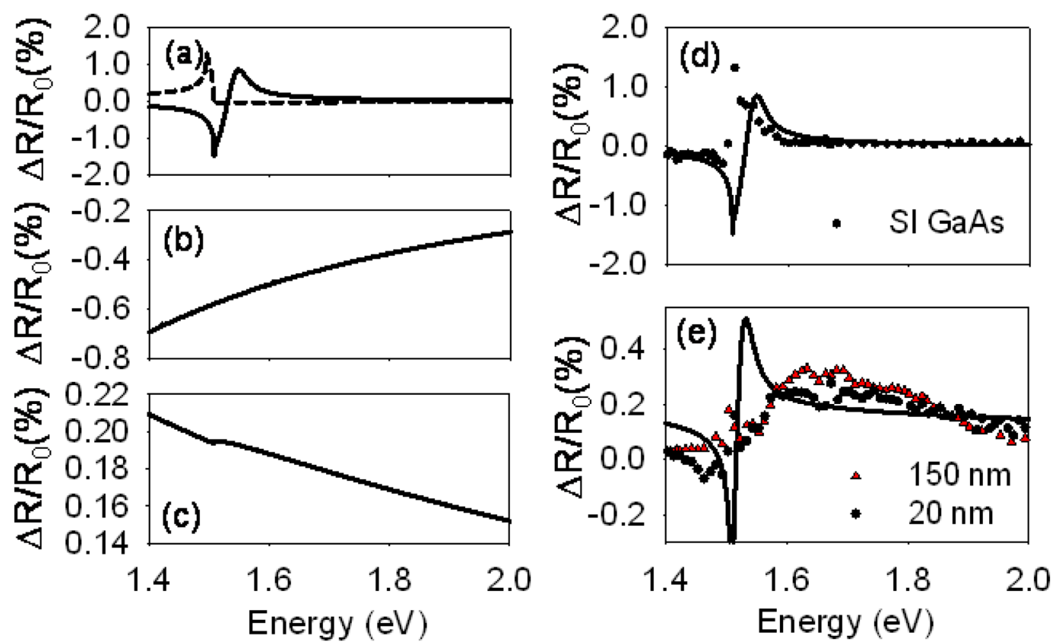

Figure 4.8: Theoretical plots of the DRR response due to (a) BGR (dashed line) and bandfilling (solid line) (b) FCA and (c) DA are shown on the left. On the right, a comparison of (d) bandfilling and the DRR response of SI GaAs at 500 ps is shown as well as (e) the DRR response of the 20 nm and 150 nm GaMnAs samples with a DRR response where bandfilling, FCA and DA are included. The strength of the DA response was the only fitting parameter used.

and consequently a larger plasma frequency than holes. For the excited carrier density in this experiment and using the electron effective mass in GaAs of $0.067m_0$, where m_0 is the mass of an electron, Eqn. 2.10 gives a plasma frequency of $\omega_p = 3.08\times10^{14}s^{-1}$. γ was taken as $1\times10^{12}s^{-1}$ reflecting experimentally measured dephasing rates [99, 100]. From the calculation of the change in extinction coefficient and change in index of refraction which contribute to the differential reflection (shown in Fig 4.7 (d, e, f)), we can see that the index of refraction dominates the contribution to the $\frac{\Delta R}{R_0}$ signal. The $\frac{\Delta R}{R_0}$ signal associated with FCA is negative and becomes increasingly large for decreasing ω. The accuracy of the FCA model is limited by the fact that the influence of defects is neglected. In addition, the effective mass model neglects the nonparabolicity of the density of states, which leads to a dependence of ω_p on the temperature of the carrier distribution. The $\frac{\Delta R}{R_0}$ signal associated with FCA at the experimental carrier density is shown in Fig. 4.8 (b).

The optical signal due to BGR was also calculated numerically using Eqn. (2.19). In calculating the BGR contribution, one needs an estimate of the magnitude of the band gap shift caused by the optically-injected carrier distribution. We used 12.6 meV, taken from [4]. Although the carrier density in [4] is smaller than our injected carrier density by a factor of 10, extrapolation of the result in [4] is nontrivial [101] and so we use the results in [4] as a guide. The calculated change in extinction coefficient and change in index of refraction due to BGR are shown in Fig. 4.7 (j, k). A sharp response just below and above the band gap are seen in the change in extinction coefficient and index of refraction respectively. The overall calculated change in $\frac{\Delta R}{R_0}$ (shown in Fig. 4.7 (f)) closely follows the change in index of refraction. The calculation shows that the BGR provides a steep positive response followed by a further decay as one moves from the band gap energy to lower energies. Above the bandgap a very small almost constant negative signal is predicted.

Figure 4.8 (d) shows the DRR response as a function of energy of SI GaAs at 500 ps along with a calculated $\frac{\Delta R}{R_0}$ curve which includes only band filling effects. As the best agreement with the experimental data is found with only state filling effects, we conclude that BGR and FCA contributions are small in SI GaAs. The dominance of state filling contributions is in agreement with the findings reported in Ref. [4]. The calculations provide reasonable agreement with the measured trends,

despite the simplicity of the theoretical model and the fact that there are no adjustable parameters in the PSF signal calculation. The discrepancy in the qualitative features, such as the magnitude of the positive and negative spike, are due to the unphysical square root density of states used in the model as discussed above. An example of a more accurate calculation by Lee et al. [4] is shown in Fig. 2.8.

The situation in GaMnAs is quite different due to the presence of defects. As discussed in Sec. 4.2, these defects lead to two modifications to the optical response relative to SI GaAs: (i) The As_{Ga} defect states can trap electrons out of the conduction band [44] (ii) Once these electrons are trapped, they induce a DA contribution to the pump probe signal. The change in extinction coefficient and index of refraction due to DA is shown in Fig. 4.7 (g, h). A broad positive response is seen in both the change in extinction coefficient and change in index of refraction. The calculated $\frac{\Delta R}{R_0}$ signal is shown in Fig. 4.7 (i). The slight bump in the $\frac{\Delta R}{R_0}$ at the band gap is due to the square root density of states function turning on the absorption coefficient sharply at the band gap energy.

In order to calculate the relative magnitude of the various signal contributions, we must estimate the fraction of the pump injected carriers trapped to defects. Since the electron trapping time is known to be a few picoseconds, we can use the relative magnitudes of the PSF signal at the band gap in LT-GaAs and SI-GaAs for delays longer than the electron trapping time to estimate the fraction of electrons trapped for the conditions of these experiments, since the residual PSF signal is caused by carriers that have not been trapped. Using the fact that the PSF signal in LT-GaAs is approximately 2.5 times smaller than band filling signal in SI GaAs, we estimated the residual carrier density by adjusting the carrier density in the calculation of the PSF to reproduce this ratio. This yielded a residual carrier density of $2 \times 10^{18}\text{cm}^{-3}$. The FCA and PSF signal contributions were then calculated for GaMnAs using this residual carrier density. The overall scaling factor A for DA, the only fitting parameter, was then adjusted to match the experimental data. No BGR contribution was included in the modeled signal as no reasonable fit could be obtained by including it, in agreement with our findings in SI-GaAs.

The calculated $\frac{\Delta R}{R_0}$ spectrum is shown in Fig. 4.8(e), along with the measured differential reflectivity spectrum at 500 ps for the two GaMnAs samples with different

thicknesses (G030-3 and F066-3). The calculated spectrum is in reasonable agreement with the measured curves. In particular, the spectra indicate a sharp onset at the band gap and a broad response above E_g. This qualitative signal shape is also consistent with the results in LT-GaAs, but only for relatively short delays due to the more rapid decay of the DA signal in that sample, as discussed in Sec. 4.1. The exact location of the onset of signal in the experimental data for GaMnAs occurs at higher photon energies than the calculated curve in Fig. 4.8 (e). Due to the signal to noise limitations in the data, the location of this onset is more easily obtained from the contour plots than in the single spectral cuts in Fig. 4.8 (e). This shift is attributed to the addition of Mn, which is not treated in the simple model we presented above. This will be further discussed in Sec. 4.4.

4.4 Discussion

In addition to providing the first comprehensive measurement of the carrier dynamics in a DMS material, the data presented in Sec. 4.2 also reveals a novel feature in the nonlinear optical response of GaMnAs that may provide insight into the electronic structure in this material. As discussed in Sec. 2.5, an active debate in the recent literature has focused on the position of the Fermi level, which may lie in the valence band or a detached impurity band. As this issue has crucial implications regarding the nature of hole transport and the mechanism of ferromagnetic coupling, it is essential that it be resolved in order that a broad understanding of the properties of DMS materials may be developed. As discussed in Sec. 2.5, this question may not be answered using linear absorption experiments at the fundamental band gap because the band gap energy is not observable due to strong contributions to the absorption from band tailing effects. Furthermore, measurements using other linear optical techniques (magnetic circular dichroism, midinfrared absorption) have yielded conflicting results. The observation of a blue shift in the onset of the $\Delta R/R_0$ signal in the GaMnAs samples relative to the SI-GaAs sample may provide insight into the position of the Fermi level. As discussed in Sec. 2.5, in p-doped semiconductors, the Fermi level resides below the edge of the valence band, implying that the energetic onset for linear absorption will occur at higher energies than in the corresponding undoped semiconductor. This is because optical transitions are only allowed between the states in

p	Hole E_F (meV)	ΔE_{g-BGR} (mev)	$\Delta E_{g-defects}$	$\Delta E_{g-Total}$
1.00E+19	33	-39	-8	-14
5.00E+19	96	-52	-21	23
1.00E+20	157	-72	-29	56
5.00E+20	459	-140	-90	229
1.00E+21	729	-170	-143	416

Table 4.1: Estimated changes to the band gap of low-temperature grown p-type GaAs due to the Moss Burstein shift, band gap renormalization and coupling to defects.

the valence band occupied by electrons and the (unoccupied) conduction band. This blue shift in the linear absorption response due to filling of the valence band states is known as the Moss Burstein shift [36, 35]. Assuming the holes in GaMnAs reside in the valence band, a rough estimate of the magnitude of the Moss Burstein shift may be obtained from a calculation of the Fermi level [102]. Since the majority (>90%) of holes will occupy the heavy hole band due to the larger effective mass, a simple one band model [77] will be reasonably accurate. The resulting values of the Fermi level are shown in the first column of Table 4.1. In a low-temperature grown, p-type semiconductor, defects also have an influence on the band gap energy. As shown in Zhang and Das Sarma in [102], coupling of carriers in the band states with impurities leads to an upward shift of the valence band edge, resulting in a reduction of the band gap. Zhang and Das Sarma also calculated the effect of exchange interactions among the holes (i.e. the BGR effect associated with the doped holes), which also produces an upward shift of the valence band edge. The results reported by Zhang and Das Sarma are also included in Table 4.1. The trends in Table 4.1 indicate that, if holes exist in the GaMnAs valence band, a net blue shift in the onset of absorption should be observed. If holes resided in a detached impurity band, the Moss Burstein effect would be absent, and a red shift of the band gap is expected. Since the magnitude of the red shifts are very sensitive to the defect distribution [102], and because the Fermi level values in Table 4.1 provide only an estimate of the Moss Burstein shift [62], only the net trend is meaningful. The observation of a net blue shift would, however, unambiguously indicate some level of valence band occupation. A direct experimental measurement of the onset of absorption would be extremely useful in assessing the position of the Fermi level.

The *nonlinear* optical technique of differential reflectivity offers several advantages

over linear optical experiments such as MCD and absorption. First, this technique is sensitive to a state filling signal associated with the optically-injected carriers, implying that states that are already filled with holes prior to excitation by the pump pulse will not produce a measured $\Delta R/R_0$ response. Secondly, the transitions below the band gap that dominate in linear spectroscopy have been shown in experiments on LT GaAs to be harder to saturate than the interband transitions [103]. The difficulty to bleach the band tail states may be the reason why a clear edge is observed in the differential reflectivity results in Fig. 4.4 and Fig. 4.6, yet no such edge is observed in the linear regime [18]. The observation of a blue shift in the onset of the differential reflectivity response of GaMnAs relative to that in GaAs supports the VB picture of the electronic structure in this material. Furthermore, our data indicate a small red shift in the nonlinear response of LT-GaAs, consistent with the presence of only defect-related band gap shifts. The magnitude of blue shift ($\sim$ 60 meV) was observed to be similar in the two GaMnAs samples studied here, which are expected to have similar hole concentrations [20], lending support to this conclusion.

It should be noted that optical transitions between the band states and the Mn_{Ga} impurity level have been shown to produce strong contributions in magnetic circular dichroism experiments [62, 24]. In an impurity band scenerio, a nonlinear state filling signal could be generated by optically-injected holes that relax into the impurity band states. The relevant transitions between the Mn_{Ga} impurity band and the conduction and valence bands are shown in Fig. 4.9. For transitions from the Mn_{Ga} level to the conduction band, the associated process would lead to a state filling response (i.e. absorption bleaching) below the band gap [104], in contrast with the blue-shifted response we observe here. Transitions from deep in the valence band to the Mn_{Ga} impurity level would create a pump-induced absorption signal that is expected to extend over a broad energy range (covering energies above and below E_g) [62, 24]. It is not clear how such a broad signal could lead to a sharp edge above the band gap of GaAs. Despite varying defect distributions and levels of compensation expected for the LT-GaAs and GaMnAs samples studied here, the pump probe signals are similar in magnitude in all cases, suggesting that additional contributions to the nonlinear response tied to the Mn_{Ga} level would be weak compared to the interband response. More theoretical work is needed to investigate the possible role of transitions between

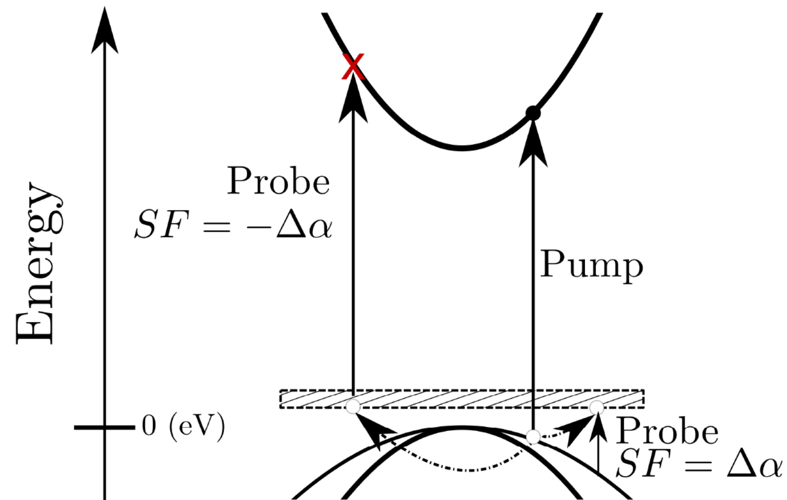

Figure 4.9: A schematic diagram of pump-induced electronic transitions in GaMnAs in the impurity band picture. After the pump excites electrons to the conduction band from the valence band, the injected holes could get trapped in the impurity band. Once there, two absorption processes could be expected: (i) a state filling signal could be expected at energies below the band gap as there would be a reduction in the available transitions from the IB to the CB; (ii) an additional absorption mechanism due to VB-IB transitions.

Mn_{Ga} impurity states and the band states in nonlinear optical experiments, such as those reported here.

Chapter 5

Conclusions and Future Work

This thesis work has encompassed the application of spectrally-resolved differential reflectivity techniques to GaMnAs in order to gain insight into the carrier dynamics and the electronic structure in this material. The experimental results reported here represent the first study of the pump probe response of a DMS semiconductor over a wide range of photon energies both above and below the semiconductor band gap. These measurements have provided considerable new insight into the trapping and relaxation dynamics in this system. Comparison of the measured results in GaMnAs with those in SI GaAs and LT GaAs, together with numerical calculations of the dominant pump probe signal contributions using a simple model, have permitted the unambiguous identification of the relevant physical processes. Free carrier absorption was found to generate a spectrally-broad, negative response during the first few picoseconds, after which the majority of free electrons ($\approx$95%, according to our analysis) are trapped into defect states. A positive signal above the band gap energy becomes dominant with the disappearance of the free carrier absorption response. As this high-energy contribution was observed to be present in all samples grown at low temperature, it was attributed to the re-excitation of electrons trapped in the As_{Ga} deep donor band by the probe pulse. Our theoretical model was shown to provide good agreement with the experimental results, indicating that state filling effects and defect-induced absorption dominate the nonlinear optical response of GaMnAs for long delays. Although many of these physical processes have been discussed in past work looking at carrier dynamics in DMS materials, the sign of the signal component associated with each contribution could not be clearly identified due to the limitation of measurements to one or a limited number of probe photon energies. Through the application of spectrally-resolved differential reflectivity experiments over a wide spectral range to GaMnAs, the spectral dependence of the key signal contributions in DMS materials has been determined in this thesis work.

The experiments carried out for this thesis work have demonstrated for the first time the utility of *nonlinear* optical techniques in providing insight into the position of the Fermi level in DMS materials. Past attempts to apply optical techniques to study this problem have used exclusively linear optical methods, which are complicated by strong background contributions. The nonlinearity of the pump probe technique makes it much less sensitive to band tail states, and consequently the measured results presented here represent the first observation of a clear edge-like feature in the optical response of a III-Mn-V DMS material. The energetic position of this edge should provide a direct optical probe of the position of the Fermi level. This thesis will therefore lay the foundation for a body of future work aimed at studying the position of the Fermi level in a wide range of samples grown under different experimental conditions and with varying Mn concentration. As such, this thesis work is expected to have considerable impact in the broader research field.

The observation of a blue shift in the differential reflectivity response of GaMnAs when compared to SI GaAs and LT GaAs lends support to the valence band picture of ferromagnetism in GaMnAs, in which the Fermi level resides in the valence band and the mechanism of ferromagnetic coupling between the Mn spins occurs through Zener Mean field interactions. Extension of these experiments to GaMnAs samples with a systematic variation in Mn concentration, similar to the linear optical studies reported in Ref [20] will be the subject of future work.

Appendix A

Excited Carrier Density Calculation Details

A.1 Spot Size Calculation

The fraction of power transmitted of a Gaussian beam of width $2w$ through a pinhole of width $2a$ is given by

$$PT = 1 - e^{-\frac{2a^2}{w^2}}, \tag{A.1}$$

where PT is the fraction of power transmitted through the pinhole [105]. This can be rearranged to yield equation 3.1, restated for clarity:

$$w = \sqrt{\frac{-2}{ln\,(1 - PT)}}a. \tag{A.2}$$

A pump power of 9.67 and 4.46 mW was measured before and after the cryostat, respectively. Since there is a 4% loss at each cryostat window-air and cryostat window-vacuum interface, this corresponds to a pump power of 8.91 mW before the pinhole and 4.84 mW after the pinhole. The pinhole has a diameter of 50 μm, yielding a spot size of 28.3 μm.

A.2 Carrier Density Calculation

For normal incidence at a vacuum-material interface of an absorbing material the reflectance is given by equation 2.7, restated for clarity:

$$R(n(\omega), \kappa(\omega)) = \frac{(n(\omega) - 1)^2 + \kappa(\omega)^2}{(n(\omega) + 1)^2 + \kappa(\omega)^2}, \tag{A.3}$$

At the pump energy, the index of refraction is given by 3.636 while the coefficient of absorption is 11200 cm^{-3}. This corresponds to an extinction coefficient of 0.0713. Substituting these values into the equation 2.7 yields a coefficient of reflectance of 0.323. Therefore, 67.6% of the energy is transmitted into the sample. The fraction

of energy transmitted through the sample is given by

$$N_{transmitted} = N_0 e^{-\alpha z}, \tag{A.4}$$

where z is the sample thickness. The fraction of the light absorbed by the sample is given by

$$\frac{N_{absorbed}}{N_0} = (1 - R)\left(1 - \frac{N_{transmitted}}{N_0}\right). \tag{A.5}$$

For a 150 nm GaAs sample, 10.5% of the incident light is absorbed. The volume excited is given by

$$V = \pi w^2 t,$$

where t is the sample thickness. The excited carrier density is given by

$$n = \frac{\text{\# of photons per pulse} \times \frac{N_{absorbed}}{N_0}}{\text{volume excited}}. \tag{A.6}$$

The number of photons per pulse is given by

$$\text{\# of photons per pulse} = \frac{\text{Pump power}}{\text{Photon energy} \times \text{Laser repetition rate}} \tag{A.7}$$

For a typical pump power of 8.91 mW, this corresponds to an excited carrier density of 3.99×10^{25} m^{-3} in a 150 nm thick GaAs sample.

Bibliography

[1] James Chelikowsky and Marvin Cohen. Nonlocal pseudopotential calculations for the electronic structure of eleven diamond and zinc-blende semiconductors. *Physical Review B*, 14(2):556–582, July 1976.

[2] H Ohno, D Chiba, F Matsukura, T Omiya, E Abe, T Dietl, Y Ohno, and K Ohtani. Electric-field control of ferromagnetism. *Nature*, 408(6815):944–946, 2000.

[3] E. Singley, K. Burch, R. Kawakami, J. Stephens, D. Awschalom, and D. Basov. Electronic structure and carrier dynamics of the ferromagnetic semiconductor Ga1-xMnxAs. *Physical Review B*, 68(16):165204, October 2003.

[4] Y. Lee, A. Chavez-Pirson, S Koch, H. Gibbs, S. Park, J Morhange, A Jeffery, N. Peyghambarian, L. Banyai, A. Gossard, and W. Wiegmann. Room-Temperature Optical Nonlinearities in GaAs. *Physical Review Letters*, 57(19):2446–2449, November 1986.

[5] H. Ohno, A. Shen, F. Matsukura, A. Oiwa, A. Endo, S. Katsumoto, and Y. Iye. (Ga,Mn)As: A new diluted magnetic semiconductor based on GaAs. *Applied Physics Letters*, 69(3):363–365, 1996.

[6] V. Novák, K. Olejník, J. Wunderlich, M. Cukr, K. Výborný, A. Rushforth, K. Edmonds, R. Campion, B. Gallagher, Jairo Sinova, and T. Jungwirth. Curie Point Singularity in the Temperature Derivative of Resistivity in (Ga,Mn)As. *Physical Review Letters*, 101(7):077201, August 2008.

[7] D Chiba, M Yamanouchi, F Matsukura, and H Ohno. Electrical manipulation of magnetization reversal in a ferromagnetic semiconductor. *Science (New York, N.Y.)*, 301(5635):943–5, August 2003.

[8] T. Wojtowicz, M. Kutrowski, G. Karczewski, J. Kossut, F. Teran, and M. Potemski. g-factor dependence of the evolution of magneto-optical spectra with the density of quasi-two-dimensional electrons in $Cd_{1-x}Mn_xTe/Cd_{1-y}Mg_yTe$ heterostructures. *Physical Review B*, 59(16):R10437–R10440, April 1999.

[9] K. Onodera, T. Masumoto, and M. Kimura. 980 nm compact optical isolators using $Cd_{1xy}Mn_xHg_yTe$ single crystals for high power pumping laser diodes. *Electronics Letters*, 30(23):1954, 1994.

[10] H. Ohno, N. Akiba, F. Matsukura, a. Shen, K. Ohtani, and Y. Ohno. Spontaneous splitting of ferromagnetic (Ga, Mn)As valence band observed by resonant tunneling spectroscopy. *Applied Physics Letters*, 73(3):363, 1998.

[11] S. Chun, S. Potashnik, K. Ku, P. Schiffer, and N. Samarth. Spin-polarized tunneling in hybrid metal-semiconductor magnetic tunnel junctions. *Physical Review B*, 66(10):20–23, September 2002.

[12] Y. Ohno, DK Young, B. Beschoten, F Matsukura, H Ohno, and DD Awschalom. Electrical spin injection in a ferromagnetic semiconductor heterostructure. *Nature*, 402(December):790–792, 1999.

[13] E. Johnston-Halperin, D. Lofgreen, R. Kawakami, D. Young, L. Coldren, a. Gossard, and D. Awschalom. Spin-polarized Zener tunneling in (Ga,Mn)As. *Physical Review B*, 65(4):1–4, January 2002.

[14] Supriyo Datta and Biswajit Das. Electronic analog of the electro-optic modulator. *Applied Physics Letters*, 56(7):665, July 1990.

[15] K. C. Hall, Wayne H. Lau, K. Gundogdu, Michael E. Flatte, and Thomas F. Boggess. Nonmagnetic semiconductor spin transistor. *Applied Physics Letters*, 83(14):2937, 2003.

[16] Kimberley C. Hall and Michael E. Flatte. Performance of a spin-based insulated gate field effect transistor. *Applied Physics Letters*, 88(16):162503, 2006.

[17] S.J. Pearton, D.P. Norton, R Frazier, S.Y. Han, C.R. Abernathy, and J.M. Zavada. Spintronics device concepts. *IEE Proceedings - Circuits, Devices and Systems*, 152(4):312–322, 2005.

[18] K. Burch, J. Stephens, R. Kawakami, D. Awschalom, and D. Basov. Ellipsometric study of the electronic structure of $Ga_{1-x}Mn_xAs$ and low-temperature GaAs. *Physical Review B*, 70(20):205208, November 2004.

[19] J. Mašek, F. Máca, J. Kudrnovský, O. Makarovsky, L. Eaves, R. Campion, K. Edmonds, A. Rushforth, C. Foxon, B. Gallagher, V. Novák, Jairo Sinova, and T. Jungwirth. Microscopic Analysis of the Valence Band and Impurity Band Theories of (Ga,Mn)As. *Physical Review Letters*, 105(22):227202, November 2010.

[20] T. Jungwirth, P. Horodyská, N. Tesarová, P. Němec, J. Šubrt, P. Malý, P. Kužel, C. Kadlec, J. Mašek, I. Němec, M. Orlita, V. Novák, K. Olejník, Z. Šobán, P. Vašek, P. Svoboda, and Jairo Sinova. Systematic Study of Mn-Doping Trends in Optical Properties of (Ga,Mn)As. *Physical Review Letters*, 105(22):227201, November 2010.

[21] T. Jungwirth, Jairo Sinova, A. MacDonald, B. Gallagher, V. Novák, K. Edmonds, A. Rushforth, R. Campion, C. Foxon, L. Eaves, E. Olejník, J. Mašek, S.-R. Yang, J. Wunderlich, C. Gould, L. Molenkamp, T. Dietl, and H. Ohno. Character of states near the Fermi level in (Ga,Mn)As: Impurity to valence band crossover. *Physical Review B*, 76(12):125206, September 2007.

[22] U Hohenester, P. Supancic, P. Kocevar, X. Zhou, W. Kütt, and H. Kurz. Subpicosecond thermalization and relaxation of highly photoexcited electrons and holes in intrinsic and p-type GaAs and InP. *Physical Review B*, 47(20):13233–13245, May 1993.

[23] K Burch, D Awschalom, and D Basov. Optical properties of III-Mn-V ferromagnetic semiconductors. *Journal of Magnetism and Magnetic Materials*, 320(23):3207–3228, December 2008.

[24] K. Ando, H. Saito, K. Agarwal, M. Debnath, and V. Zayets. Origin of the Anomalous Magnetic Circular Dichroism Spectral Shape in Ferromagnetic Ga1-xMnxAs: Impurity Bands inside the Band Gap. *Physical Review Letters*, 100(6):067204, February 2008.

[25] W.-Z. Lin, R.W. Schoenlein, J.G. Fujimoto, and E.P. Ippen. Femtosecond absorption saturation studies of hot carriers in GaAs and AlGaAs. *IEEE Journal of Quantum Electronics*, 24(2):267–275, 1988.

[26] P C Becker, H. L. Fragnito, C. H. Brito Cruz, J. Shah, R L Fork, J. E. Cunningham, J. E. Henry, and C V Shank. Femtosecond intervalley scattering in GaAs. *Applied Physics Letters*, 53(21):2089–2090, 1988.

[27] D. von der Linde and R. Lambrich. Direct Measurement of Hot-Electron Relaxation by Picosecond Spectroscopy. *Physical Review Letters*, 42(16):1090–1093, April 1979.

[28] E Beaurepaire, J Merle, a Daunois, and J Bigot. Ultrafast spin dynamics in ferromagnetic nickel. *Physical review letters*, 76(22):4250–4253, May 1996.

[29] J. Güdde, U. Conrad, V. Jähnke, J. Hohlfeld, and E. Matthias. Magnetization dynamics of Ni and Co films on Cu(001) and of bulk nickel surfaces, March 1999.

[30] M. Woerner, A. Lohner, T. Elsaesser, and W. Kaiser. Capture of hot holes by shallow acceptors in p-type GaAs studied by picosecond infrared spectroscopy. *Physical Review B*, 47(19):12498–12509, May 1993.

[31] H. D. Chen, M. S. Feng, K. C. Lin, P. A. Chen, C. C. Wu, and J. W. Wu. Anomalous mobility enhancement in heavily carbon-doped GaAs. *Journal of Applied Physics*, 75(10):5453–5455, 1994.

[32] Marshall Nathan, Gerald Burns, Samuel Blum, and John Marinace. Electroluminescence and Photoluminescence of GaAs at 77K. *Physical Review*, 132(4):1482–1485, November 1963.

[33] C. Persson, R. Ahuja, and B. Johansson. Full band calculation of doping-induced band-gap narrowing in p-type GaAs. *Physical Review B*, 64(3):033201, June 2001.

[34] Bo Sernelius. Band-gap shifts in heavily p-type doped semiconductors of the zinc-blende and diamond type. *Physical Review B*, 34(8):5610–5620, October 1986.

[35] T S Moss. The Interpretation of the Properties of Indium Antimonide. *Proceedings of the Physical Society. Section B*, 67(10):775–782, October 1954.

[36] Elias Burstein. Anomalous Optical Absorption Limit in InSb. *Physical Review*, 93(3):632–633, February 1954.

[37] H. C. Casey, D. D. Sell, and K. W. Wecht. Concentration dependence of the absorption coefficient for n- and p-type GaAs between 1.3 and 1.6 eV. *Journal of Applied Physics*, 46(1):250–257, 1975.

[38] H. C. Casey. Concentration-dependent absorption and spontaneous emission of heavily doped GaAs. *Journal of Applied Physics*, 47(2):631–643, 1976.

[39] H.S. Loka, S.D. Benjamin, and P.W.E. Smith. Optical characterization of low-temperature-grown GaAs for ultrafast all-optical switching devices. *IEEE Journal of Quantum Electronics*, 34(8):1426–1437, 1998.

[40] D C Look, D C Walters, and G D Robinson. D. C. Look, D. C. Walters, and G. D. Robinson. pages 306–310, 1993.

[41] N. Hozhabri, S.-H. Lee, and K. Alavi. Erratum: Infrared measurements in annealed molecular beam epitaxy GaAs grown at low temperature [Appl. Phys. Lett. 66, 2546 (1995)]. *Applied Physics Letters*, 66(19):2546–2548, 1995.

[42] G. Segschneider, T. Dekorsy, H. Kurz, R. Hey, and K. Ploog. Energy resolved ultrafast relaxation dynamics close to the band edge of low-temperature grown GaAs. *Applied Physics Letters*, 71(19):2779–2781, 1997.

[43] P. Silverberg, P. Omling, and L Samuelson. Hole photoionization cross sections of EL2 in GaAs. *Applied Physics Letters*, 52(20):1689, 1988.

[44] P. W. E Smith, S. D. Benjamin, and H. S. Loka. Tailoring of trap-related carrier dynamics in low-temperature-grown GaAs. *Applied Physics Letters*, 71(9):1156–1158, 1997.

[45] D. Streb. Optical characterization of low temperature grown GaAs by transmission measurements above the band gap. *Journal of Vacuum Science*, 14(3):2275–2277, May 1996.

[46] S. U. Dankowski, P. Kiesel, B. Knupfer, M. Kneissl, G. H. Dohler, U. D. Keil, D. R. Dykaar, and R. F. Kopf. Annealing induced refractive index and absorption changes of low-temperature grown GaAs. *Applied Physics Letters*, 65(25):3269–3271, 1994.

[47] A. Chantre, G. Vincent, and D. Bois. Deep-level optical spectroscopy in GaAs. *Physical Review B*, 23(10):5335–5359, May 1981.

[48] A. Van Esch, J. De Boeck, G. Verbanck, a. S. van Steenbergen, P. J. Wellmann, B. Grietens, R. Bogaerts, F. Herlach, and G. Borghs. Interplay between the magnetic and transport properties in the III-V diluted magnetic semiconductor $Ga_{1-x}Mn_xAs$. *Physical Review B*, 56(20):13103–13112, November 1997.

[49] N.A. Spaldin. *Magnetic Materials: Fundamentals and Applications*. Cambridge University Press, 2010.

[50] M. Linnarsson, E. Janzén, B. Monemar, M. Kleverman, and A. Thilderkvist. Electronic structure of the GaAs:Mn_{Ga} center. *Physical Review B*, 55(11):6938–6944, March 1997.

[51] M. Poggio, R. Myers, N. Stern, A. Gossard, and D. Awschalom. Structural, electrical, and magneto-optical characterization of paramagnetic GaMnAs quantum wells. *Physical Review B*, 72(23):235313, December 2005.

[52] C. Zener. Interaction Between the d Shells in the Transition Metals. *Physical Review*, 81(3):440–444, February 1951.

[53] T. Dietl. Zener Model Description of Ferromagnetism in Zinc-Blende Magnetic Semiconductors. *Science*, 287(5455):1019–1022, 2000.

[54] S. Koshihara, A. Oiwa, M. Hirasawa, S. Katsumoto, Y. Iye, C. Urano, H. Takagi, and H. Munekata. Ferromagnetic Order Induced by Photogenerated Carriers in Magnetic III-V Semiconductor Heterostructures of (In,Mn)As/GaSb. *Physical Review Letters*, 78(24):4617–4620, June 1997.

[55] T. Dietl. Hole-mediated ferromagnetism in tetrahedrally coordinated semiconductors. *Physical Review B*, 63(19):195205, April 2001.

[56] Tomasz Dietl. Ferromagnetic semiconductors. *Semiconductor Science and Technology*, 17(4):377–392, April 2002.

[57] H. Akai. Ferromagnetism and Its Stability in the Diluted Magnetic Semiconductor (In, Mn)As. *Physical Review Letters*, 81(14):3002–3005, October 1998.

[58] A.. Chattopadhyay, S. Das Sarma, and A. Millis. Transition Temperature of Ferromagnetic Semiconductors: A Dynamical Mean Field Study. *Physical Review Letters*, 87(22):227202, November 2001.

[59] G. Alvarez and E. Dagotto. Single-band model for diluted magnetic semiconductors: Dynamical and transport properties and relevance of clustered states. *Physical Review B*, 68(4):045202, July 2003.

[60] S.-R. Yang and A. MacDonald. Disorder and ferromagnetism in diluted magnetic semiconductors. *Physical Review B*, 67(15):155202, April 2003.

[61] B. Sheu, R. Myers, J.-M. Tang, N. Samarth, D. Awschalom, P. Schiffer, and M. Flatté. Onset of Ferromagnetism in Low-Doped Ga1-xMnxAs. *Physical Review Letters*, 99(22):227205, November 2007.

[62] Jian-Ming Tang and Michael Flatté. Magnetic Circular Dichroism from the Impurity Band in III-V Diluted Magnetic Semiconductors. *Physical Review Letters*, 101(15):157203, October 2008.

[63] Jian-Ming Tang and Michael Flatté. Multiband Tight-Binding Model of Local Magnetism in $Ga_{1-x}Mn_xAs$. *Physical Review Letters*, 92(4):047201, January 2004.

[64] E. Singley, R. Kawakami, D. Awschalom, and D. Basov. Infrared Probe of Itinerant Ferromagnetism in $Ga_{1-x}Mn_xAs$. *Physical Review Letters*, 89(9):097203, August 2002.

[65] K. Burch, D. Shrekenhamer, E. Singley, J. Stephens, B. Sheu, R. Kawakami, P. Schiffer, N. Samarth, D. Awschalom, and D. Basov. Impurity Band Conduction in a High Temperature Ferromagnetic Semiconductor. *Physical Review Letters*, 97(8):087208, August 2006.

[66] G. Acbas, M.-H. Kim, M. Cukr, V. Novák, M. Scarpulla, O. Dubon, T. Jungwirth, Jairo Sinova, and J. Cerne. Electronic Structure of Ferromagnetic Semiconductor Ga1-xMnxAs Probed by Subgap Magneto-optical Spectroscopy. *Physical Review Letters*, 103(13):137201, September 2009.

[67] Kang-Jeon Han, Ji-Hee Kim, Ki-Ju Yee, X. Liu, J. K. Furdyna, and F. Hache. Magnetization-induced optical nonlinearity in ferromagnetic GaMnAs. *Journal of Applied Physics*, 101(6):063519, 2007.

[68] Y. Mitsumori, A. Oiwa, T. Slupinski, H. Maruki, Y. Kashimura, F. Minami, and H. Munekata. Dynamics of photoinduced magnetization rotation in ferromagnetic semiconductor p-(Ga,Mn)As. *Physical Review B*, 69(3):033203, January 2004.

[69] Shin Kim, Eunsoon Oh, J. U. Lee, D. S. Kim, S. Lee, and J. K. Furdyna. Effect of point defect and Mn concentration in time-resolved differential reflection in GaMnAs. *Applied Physics Letters*, 88(26):262101, 2006.

[70] Shin Kim, Eunsoon Oh, J. U. Lee, D. S. Kim, S. Lee, and J. K. Furdyna. Time-resolved differential reflection measurements on GaMnAs grown by molecular beam epitaxy. *Physica Status Solidi (C)*, 2(8):3141–3144, May 2005.

[71] Shin Kim, Eunsoon Oh, J. U. Lee, D. S. Kim, S. Lee, and J. K. Furdyna. Time-resolved differential reflection measurements on GaMnAs grown by molecular beam epitaxy. *Journal of the Korean Physical Society*, 49(4):1611–1614, May 2006.

[72] K. J. Yee, D. Lee, X. Liu, W. L. Lim, M. Dobrowolska, J. K. Furdyna, Y. S. Lim, K. G. Lee, Y. H. Ahn, and D. S. Kim. Optical studies of carrier and phonon dynamics in $Ga_{1-x}Mn_xAs$. *Journal of Applied Physics*, 98(11):113509, 2005.

[73] Ji-Hee Kim, Kang-Jeon Han, Dong-Wook Jang, Ki-Ju Yee, X. Liu, and J. K. Furdyna. Spin-Polarized Photoreflectance in Ferromagnetic GaMnAs. *Journal of the Korean Physical Society*, 50(3):819–823, March 2007.

[74] E. Rozkotova, P. Nemec, D. Sprinzl, P. Horodyska, F. Trojanek, P. Maly, V. Novak, K. Olejnik, M. Cukr, and T. Jungwirth. Laser-Induced Precession of Magnetization in GaMnAs. *IEEE Transactions on Magnetics*, 44(11):2674–2677, November 2008.

[75] E. Kojima, R. Shimano, Y. Hashimoto, S. Katsumoto, Y. Iye, and M. Kuwata-Gonokami. Observation of the spin-charge thermal isolation of ferromagnetic $Ga_{0.94}Mn_{0.06}As$ by time-resolved magneto-optical measurements. *Physical Review B*, 68(19):193203, November 2003.

[76] E. Kojima, J. Héroux, R. Shimano, Y. Hashimoto, S. Katsumoto, Y. Iye, and M. Kuwata-Gonokami. Experimental investigation of polaron effects in $Ga_{1-x}Mn_xAs$ by time-resolved and continuous-wave midinfrared spectroscopy. *Physical Review B*, 76(19):195323, November 2007.

[77] C. Kittel. *Introduction to solid state physics*. Wiley, 2005.

[78] B. Van Zeghbroeck. *Principles of Semiconductor Devices*. University of Colorago at Boulder, http://ecee.colorado.edu/˜bart/book//, 2007.

[79] D. C. Hutchings, M. Sheik-Bahae, D. J. Hagan, and E. W. Stryland. Kramers-Krönig relations in nonlinear optics. *Optical and Quantum Electronics*, 24(1):1–30, January 1992.

[80] Henry van Driel. *Modern Optics and Laser Physics*. University of Toronto, 1992.

[81] H. Haug and S.W. Koch. *Quantum theory of the optical and electronic properties of semiconductors*. World Scientific, 2009.

[82] T. Jungwirth, P. Horodyská, N. Tesarová, P. Němec, J. Šubrt, P. Malý, P. Kužel, C. Kadlec, J. Mašek, I. Němec, M. Orlita, V. Novák, K. Olejník, Z. Šobán, P. Vašek, P. Svoboda, and Jairo Sinova. Systematic Study of Mn-Doping Trends in Optical Properties of (Ga,Mn)As (Supplement). *Physical Review Letters*, 105(22):227201, November 2010.

[83] P. Vašek, P. Svoboda, V. Novák, M. Cukr, Z. Výborný, V. Jurka, J. Stuchlík, M. Orlita, and D. K. Maude. Anisotropic Magnetoresistance of GaMnAs Ferromagnetic Semiconductors. *Journal of Superconductivity and Novel Magnetism*, 23(6):1161–1163, January 2010.

[84] A. H. MacDonald, P. Schiffer, and N. Samarth. Ferromagnetic semiconductors: moving beyond (Ga,Mn)As. *Nature Materials*, 4(3):195–202, March 2005.

[85] J. Kunde, S. Arlt, L. Gallmann, F. Morier-Genoud, U. Siegner, and U. Keller. Sensitive characterization of phase and amplitude semiconductor nonlinearities for broadband 20 fs excitation. *Journal of Applied Physics*, 88(2):1187–1189, 2000.

[86] A Alexandrou, V. Berger, and D. Hulin. Direct observation of electron relaxation in intrinsic GaAs using femtosecond pump-probe spectroscopy. *Physical Review B*, 52(7):4654–4657, August 1995.

[87] S Hunsche, H Heesel, a Ewertz, H Kurz, and Jh Collet. Spectral-hole burning and carrier thermalization in GaAs at room temperature. *Physical review. B, Condensed matter*, 48(24):17818–17826, December 1993.

[88] J. Shah. *Ultrafast spectroscopy of semiconductors and semiconductor nanostructures*. Springer series in solid-state sciences. Springer, 1999.

[89] A. J. Taylor, D. J. Erskine, and C. L. Tang. Ultrafast relaxation dynamics of photoexcited carriers in GaAs and related compounds. *Journal of the Optical Society of America B*, 2(4):663–673, April 1985.

[90] A. J. Lochtefeld, M. R. Melloch, J. C. P. Chang, and E. S. Harmon. The role of point defects and arsenic precipitates in carrier trapping and recombination in low-temperature grown GaAs. *Applied Physics Letters*, 69(10):1465–1467, 1996.

[91] Y. Kostoulas, L. J. Waxer, I. a. Walmsley, G. W. Wicks, and P. M. Fauchet. Femtosecond carrier dynamics in low-temperature-grown indium phosphide. *Applied Physics Letters*, 66(14):1821–1823, 1995.

[92] S Gupta, M Y Frankel, J A Valdmanis, J F Whitaker, G. A. Mourou, F. W. Smith, and A. R. Calawa. Subpicosecond carrier lifetime in GaAs grown by molecular beam epitaxy at low temperatures. *Applied Physics Letters*, 59(25):3276–3278, 1991.

[93] U. Siegner, R. Fluck, G. Zhang, and U. Keller. Ultrafast high-intensity nonlinear absorption dynamics in low-temperature grown gallium arsenide. *Applied Physics Letters*, 69(17):2566–2568, 1996.

[94] J. Kuhl, E. O. Gobel, Th. Pfeiffer, and A. Jonietz. Subpicosecond carrier trapping in high-defect-density amorphous Si and GaAs. *Applied Physics A Solids and Surfaces*, 34(2):105–110, June 1984.

[95] A. Krotkus, K. Bertulis, M. Kaminska, K. Korona, A. Wolos, J. Siegert, S. Marcinkevicius, J.-F. Roux, and J.-L. Coutaz. Be-doped low-temperature-grown GaAs material for optoelectronic switches. *IEE Proceedings - Optoelectronics*, 149(3):111–115, 2002.

[96] J. P. Zahn, a. Gamouras, S. March, X. Liu, J. K. Furdyna, and K. C. Hall. Ultrafast studies of carrier and magnetization dynamics in GaMnAs. *Journal of Applied Physics*, 107(3):033908, 2010.

[97] J. Wang, Y. Hashimoto, J. Kono, A. Oiwa, H. Munekata, G. Sanders, and C. Stanton. Propagating coherent acoustic phonon wave packets in $In_xMn_{1-x}As$/GaSb. *Physical Review B*, 72(15):153311, October 2005.

[98] M. Sturge. Optical Absorption of Gallium Arsenide between 0.6 and 2.75 eV. *Physical Review*, 127(3):768–773, August 1962.

[99] J. L. Oudar, A. Migus, D. Hulin, G. Grillon, J. Etchepare, and A. Antonetti. Femtosecond orientational relaxation of photoexcited carriers in gaas. *Phys. Rev. Lett.*, 53:384–387, Jul 1984.

[100] P. C. Becker, H. L. Fragnito, C. H. Brito Cruz, R. L. Fork, J. E. Cunningham, J. E. Henry, and C. V. Shank. Femtosecond photon echoes from band-to-band transitions in gaas. *Phys. Rev. Lett.*, 61:1647–1649, Oct 1988.

[101] L. Banyai and S. W. Koch. Banyai and koch reply. *Phys. Rev. Lett.*, 60(12):1206, Mar 1988.

[102] Ying Zhang and S. Das Sarma. Temperature and magnetization-dependent band-gap renormalization and optical many-body effects in diluted magnetic semiconductors. *Physical Review B*, 72(12):125303, September 2005.

[103] M. Haiml, U. Siegner, F. Morier-Genoud, U. Keller, M. Luysberg, R. C. Lutz, P. Specht, and E. R. Weber. Optical nonlinearity in low-temperature-grown GaAs: Microscopic limitations and optimization strategies. *Applied Physics Letters*, 74(21):3134, 1999.

[104] A. Lohner, M. Woerner, T. Elsaesser, and W. Kaiser. Picosecond capture of photoexcited holes by shallow acceptors in p-type GaAs. *Physical Review Letters*, 68(26):3920–3923, June 1992.

[105] A.E. Siegman. *Lasers*. University Science Books, 1986.